Exploring the role of nuclear transport and chromatin state in micronucleus stability

Molly Grace Zych

A dissertation
submitted in partial fulfillment of the
requirements for the degree of

Doctor of Philosophy

University of Washington
2024

Reading Committee:
Emily Hatch, Chair
Susan Parkhurst
Brian Beliveau

Program Authorized to Offer Degree:
Molecular and Cellular Biology

University of Washington

Abstract

Exploring the role of nuclear transport and chromatin state in micronucleus stability

Molly G. Zych

Chair of the Supervisory Committee:
Emily Hatch
Department of Biochemistry

Micronuclei (MN) form when missegregated chromatin recruits its own nuclear envelope after mitosis. MN are byproducts of genome instability, are defective in performing most nuclear functions, and cause further aneuploidy and DNA damage. MN are unstable and their rupture can activate immune signaling and metastatic pathways, contributing to cancer progression. Many studies have identified mechanisms that contribute to MN rupture. Defects in nuclear envelope protein recruitment lead to rupture and are influenced by spindle position or chromosome identity. Chromosome size influences MN stability through lamin B1 and nuclear pore complex recruitment, while gene density influences stability through lamina organization, though the mechanism behind this is not known. While most nuclear functions are altered in MN, it's still not well understood how or if these erroneous functions also contribute to MN rupture.

In this work, I first investigate how gene density influences the stability of small MN, MN containing short chromosomes, in Chapter 2. I find that histone modifications are influential on small MN rupture, where heterochromatin contributes to lamina gaps and instability. This occurs

through nuclear growth, which is largely influenced by nuclear transport and recruitment of RCC1, a RanGEF. Euchromatic MN, which are stable, are especially depleted for RCC1, whereas heterochromatic MN have higher RCC1 recruitment. In addition to this defect in small MN, I identify growth as a new contributor to MN rupture and find that all MN have an export defect that leads to growth, lamina gap formation, and rupture. I analyzed existing chromothripsis data from patients and found that chromothripsis on early rupturing chromosomes contains higher levels of APOBEC mutations compared to late rupturing chromosomes, suggesting rupture timing is important for MN consequences. Additional work summarized in Chapter 3 looks into the mechanisms responsible for MN formation. I determined MN content after spindle assembly checkpoint inhibition or merotelic microtubule attachment and found that MN content is non-random and specific to the mechanism of formation. Additional unfinished work developed tools to identify MN content in a high throughput manner, either through subcellular fractionation or multiplexed DNA-FISH.

Together these studies help define how chromosome identity influences MN formation, function, rupture, and the consequences of MN rupture. This work suggests that the previously identified defects in MN function are more variable than previously appreciated and that these differences can influence the contribution MN make to long lasting cellular consequences. Future studies should look further into the cause of the transport defects in MN, better define what triggers MN rupture, and test the role of these mechanisms of MN rupture in vivo.

Table of Contents

List of Figures 7

Acknowledgements 8

Chapter 1 : Introduction 10

- Micronucleus formation 10
- Micronucleus rupture and its consequences 11
- Defects in intact micronuclei 14
- Nuclear transport defects in micronuclei: a mechanism driving functional change 18
- Chromatin content determines micronucleus structure and function 19
- Concluding remarks and perspectives: 21
- Thesis overview 22

Chapter 2 : Nuclear transport drives micronucleus disruption 23

- Abstract 23
- Introduction 24
- Results 25
- Discussion 46
- Methods 49

Chapter 3 : The contribution of chromosome identity to micronucleus formation 63

- Abstract 63
- Introduction 63
- Results 65
- Discussion 69
- Methods 71

Chapter 4 : Conclusions and future directions 75

- The influence of gene density on MN stability 75
- The origin of lamina gaps in MN 75
- Defective nuclear export in MN 76
- MN rupture in cancer 77
- Conclusions 78

References 79

Appendix A: Supplementary material for Chapter 2 89

Supplementary Figures 89

List of Figures

Figure 1.1: The disruption of nuclear functions in intact and ruptured micronuclei. 14

Figure 1.2: The influence of chromosome features on missegregation and micronucleation. 20

Figure 2.1: Histone modifications regulate small MN stability 29

Figure 2.2: MN size correlates with histone modifications and stability 33

Figure 2.3: MN overgrow due to a defect in nuclear export... 37

Figure 2.4: High euchromatin leads to additional defects in MN import 39

Figure 2.5: Defects in RCC1 recruitment result in decreased nuclear export in MN 43

Figure 2.6: APOBEC signatures are enriched in early rupture chromosome chromothripsis events... 45

Figure 3.1: Non-random micronucleation of human chromosomes.. 67

Figure 3.2: TigerFISH validation.. 68

Supplementary Figure 2.1: Manipulation of histone modifications and transcription in nuclei and MN 90

Supplementary Figure 2.2: Lamina gaps and instability in MN correlate with growth not LADs 91

Supplementary Figure 2.3: MN transport rates are conserved and not correlated with MN area 93

Supplementary Figure 2.4: RCC1 levels more than NUP density correlate with export defects in MN... 96

Supplementary Figure 2.5: Controls for chromothripsis analysis 97

Acknowledgements

The work in this thesis would not have been possible without the support from many people, both in and outside of the lab. First to Emily, thank you so much for letting me join your lab and being such a great scientific role model for me the past 6 years. I was lucky to join the Hatch lab early in its existence and to be trained by Emily directly. I have learned so much about designing and performing experiments from Emily, but I am especially thankful for how I've learned to think about and communicate science from you. Outside of scientific mentorship, thank you for being such a supportive mentor and helping me get through the emotional rollercoaster that is graduate school, especially the last few years. I am so grateful for all that I have learned from you and your continued support.

To the other members of the Hatch lab over the years, I am thankful for the help, inspiration, and friendship you have given me. To Amanda, who was such a great leader within our lab, the best person to talk about data with, and everyone's biggest cheerleader. You also were the first person to say 'good morning sunshine' to us every day and were such a positive spirit that kept us all motivated and excited about our work. I learned so much from you, and your belief in me made me believe in myself more than I could have on my own. To Anna, who was a fellow micronucleus researcher while in the lab, thank you for being a mentor to me when I first joined the lab and always being willing to grab a coffee and chat about our current models for each of our projects. And last to Maya, who has been my sole lab mate for the past 5 months, thank you for helping me push this project across the finish line.

Outside of lab, I have been lucky to find amazing friends in Seattle that made my time in grad school so much more than simply an educational experience. To my MCB cohort, I am so glad I got to have such a great group of people to learn the ropes of grad school with. To my roommates (even though we haven't lived together in a few years I will always call you roommates) Hannah and Laila. I can't believe we did not know each other 6 years ago because I really would not be who I am now without knowing you two. You were such great role models to me and amazing friends to talk through the daily ups and downs of grad school with. To Hannah, I so miss our morning chats over coffee and walking to work together. Thank you for being such a good friend to me, I have loved being able to take adventures together during our time in Seattle and look forward to more in the future. Through the narrowing of social groups during covid, I was fortunate to form a group of close friends, the Zoo squad, who became my family in Seattle. Thank you all so much for everything: the big group trips, causal evenings drinking on our patio, family dinners, floats in lake union, nights playing darts at the zoo, and every little thing in between. Everyone has moved on to a new position in their own corner of the country and I am so excited to visit you all in your new homes. I also want to thank Andie and Logan, who have become 2 of my best friends these past few years and who let me be in their home almost as much as I was at my own the past year. You guys kept me company during the most stressful parts of putting together this thesis and reminded me to remember my life outside of my thesis at times when I needed that reminder.

Last, I want to thank my family. My dad is the most selfless person I know. My mom is hardworking and kind. You both taught me the resilience and kindness I needed to make it to this point in my career. Thank you so much for constantly supporting me while I have been far from home over the past 6 years. Especially to my mom, who has taken my daily phone calls over the past few months, your love and support made it possible for me to finish this degree. To my sister Meghan and brother-in-law John, thank you for being the best support system to come home to. Meghan you were my first role model. Thank you for being so loving, passionate, and warmhearted. Since I have been in school you got married, bought a house, and had 2 kids, and I have loved being able to be celebrate each of these milestones with you. To Zeke and Isabelle, you guys are too young to know it yet, but you are such rays of light in my life. I love watching you grow up and can’t wait to be closer to home to see you all more often.

Chapter 1 : Introduction

Sections of text in this chapter have been modified from the following manuscript:

Zych MG, Hatch EM. Small spaces, big problems: The abnormal nucleoplasm of micronuclei and its consequences. Curr Opin Struct Biol. 2024 Aug;87:102839. doi: 10.1016/j.sbi.2024.102839. Epub 2024 May 18. PMID: 38763098.

Micronucleus formation

The nuclear envelope (NE) is composed of a double membrane, nuclear pore complexes (NPCs) that span the membranes, a meshwork of nuclear lamin filaments associated with the inner nuclear membrane (INM), and a collection of membrane associated proteins, called NETs, that link the INM to the lamin meshwork and peripheral chromatin. The NE is a critical barrier that separates the nucleus from the cytoplasm, with NPCs regulating the passage of molecules between compartments, and that preserves the structural integrity of the genome through multiple mechanisms. During mitosis in metazoans, the NE disassembles to allow proper chromosome alignment and segregation. After chromosome segregation, NETs in the ER, lamin proteins, and NPCs are sequentially recruited to the chromatin in a cell type specific manner [1] to reform the NE and recreate the barrier between the nucleus and cytoplasm. When NE assembly occurs on chromatin outside of the main chromatin mass, including chromatin fragments or lagging chromosomes, micronuclei (MN) form.

MN formation results from several types of genome instability, including mitotic errors causing whole chromosome missegregation and DNA damage or DNA replication errors causing acentric fragment formation. This strong association with chromosome instability and DNA damage has led to their use as biomarkers of carcinogen exposure and cancer [2]. Recent work has highlighted how MN also result from changes in ER organization [3–5], suggesting that they could also be a sensitive readout of broader changes in cellular architecture. The frequency with which missegregating chromatin becomes a MN varies widely between cell types [6,7] and can be mitigated by an anaphase surveillance system, based on Aurora B signaling, that delays NE resealing [8,9]. Despite this, MN occur regularly in somatic cells due to stochastic mitotic errors [10]. They are observed in a variety of healthy epithelial tissues [11] and increase in frequency in cancer tissues, during aging, and in certain pathological conditions, including autoimmune, neurodegenerative, and laminopathy diseases [10,12–15]. An extensive list of conditions characterized by increased MN and the potential contributions of MN to their pathology can be found in a recent review [10].

Micronucleus rupture and its consequences

MN frequently undergo membrane rupture and rarely undergo membrane repair, resulting in a loss of compartmentalization that exposes chromatin to the cytoplasm for the rest of interphase. In some cell lines, MN rupture frequency can reach as high as 90% during interphase arrest [16]. There are still many questions about the mechanism of MN rupture and what prevents its repair. What is known is that membrane rupture is enhanced by defects in NE structure in MN [16]. MN frequently fail to properly recruit key NE proteins, including lamin B1 and NPCs, during mitotic exit and early G1, which is thought to lead to gaps in the lamina that become sites of membrane rupture [16,17]. In addition, recent work found that aberrant activation of the ATR kinase in MN depletes lamin A/C from the NE, which increases rupture in a subset of MN [18]. Whether lamina disruption, through issues with lamin recruitment, maintenance, and/or premature disassembly, is the main cause of MN rupture, or if there are additional processes that trigger membrane disruption is still unclear. After rupture, MN recruit many of the proteins required for post-mitotic NE assembly and nuclear membrane rupture repair, yet they ultimately fail to recompartmentalize. The current model is that over-recruitment of the ESCRT-III membrane remodeling complex to ruptured MN leads to ER invasion, persistent disruption, and even DNA damage, instead of membrane resealing [19,20]. However, the mechanistic details of this remain to be defined.

Much of the current interest in MN is driven by ground-breaking work demonstrating that MN and MN rupture are potent causes of massive genome instability events thought to drive both cancer initiation and metastasis [21] and triggers of inflammatory and invasion pathway upregulation [22]. Current research has identified several factors that can cause DNA damage in both intact and ruptured MN. Defective transcription in intact MN can cause R-loop formation and the subsequent recruitment of the nickase APE1 causing interphase DNA damage [23]. In addition, delayed DNA replication in intact MN can drive DNA damage through the action of error prone DNA-polymerases during mitosis [24,25]. Ruptured MN are exposed to cytosolic nucleases, including TREX1, which can cause DNA fragmentation and double-stranded (dsDNA) breaks [26]. Exposed DNA ends in damaged MN are also substrates for APOBEC-dependent mutation [27]. During mitosis fragmented MN DNA is held together by CIP2A-TOPBP1 complexes [28] and repaired into highly reorganized and mutated chromosomes in the next cell cycle in a process called chromothripsis [29]. Detailed discussion of these mechanisms can be found in several excellent reviews [30,31].

Upon rupture, MN chromatin frequently recruits the innate immune activator, cGAS [32,33]. However, whether this binding induces an innate immune response is still under investigation [34,35]. Early studies found cGAS-STING signaling occurred, but well after MN formation and rupture, perhaps even after the next mitosis [32,33]. Additional work has found that several mechanisms active on ruptured MN, including the binding of BAF (barrier to autointegration factor) [36] and TREX1 activity [26], are sufficient to inhibit cGAS activation. A recent, direct analysis of cGAS recruitment to MN suggests that activity may also depend on the state of the exposed chromatin [37]. Clarifying the requirements for cGAS activation on MN will be a key area of research in the coming years to truly understand the frequency with which MN activate these pathways in cancer.

Several excellent reviews on MN formation and the consequences of MN rupture have been published recently [30,38,39]. Here, I highlight evidence that intact MN lack a fully functional nuclear environment (Fig. 1.1), leading to significant consequences for the enclosed chromatin and the cell. In addition, I discuss recent findings of biased chromosome missegregation into MN and the impact on MN function and stability. Together these studies demonstrate that there is a need to define the nuclear environment in MN, both chromosome content and nuclear function, to better understand how alterations to nuclear function may contribute to MN instability.

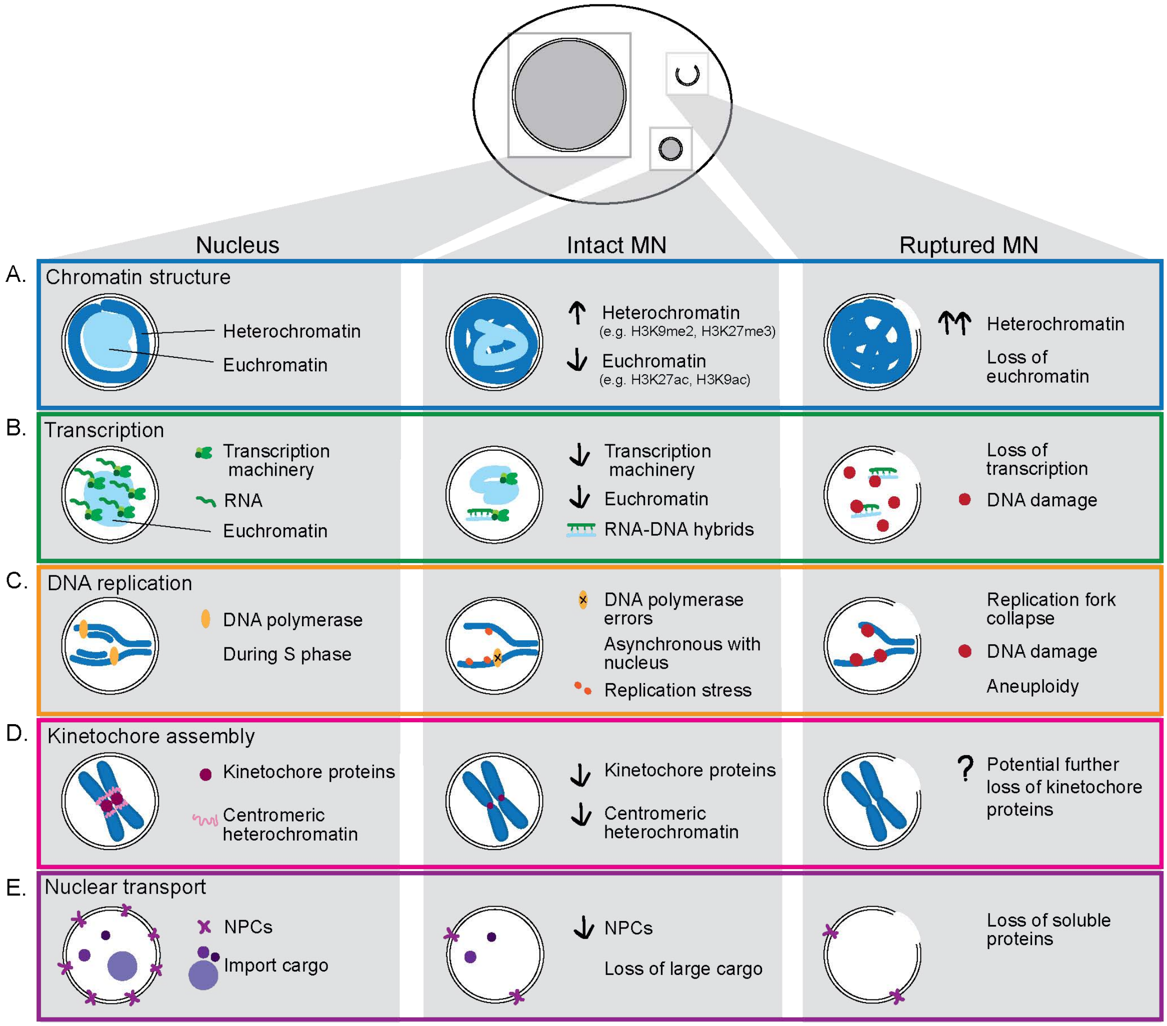

Figure 1.1: The disruption of nuclear functions in intact and ruptured micronuclei.

A. Intact micronuclei (MN) have overcompacted chromatin, are enriched for heterochromatin modifications, and are depleted for euchromatin modifications. Ruptured MN lose euchromatin modifications completely and have a further enrichment of heterochromatin modifications. **B.** Intact MN have decreased mRNA production, decreased euchromatin, are depleted for multiple essential transcription proteins, and form RNA-DNA hybrids. Ruptured MN lose the ability to transcribe mRNA and persistence of RNA-DNA hybrids causes DNA damage. **C.** Intact MN have error prone DNA polymerases, replicate their DNA asynchronously from the nucleus, and undergo replication stress. MN rupture halts DNA replication, leading to aneuploidy, collapsed replication forks, and DNA damage. **D.** Intact MN are depleted for kinetochore proteins and have reduced centromeric heterochromatin. Ruptured MN may have further defects in kinetochore assembly. **E.** Intact MN have a decreased density of NPCs and are lacking many nuclear proteins, especially large proteins. MN rupture results in loss of all soluble proteins due to a lack of compartmentalization from the cytoplasm.

Defects in intact micronuclei

Chromatin structure

The NE has essential functions in chromatin organization, including heterochromatin binding at the nuclear periphery and regulating transport of histone modifying enzymes. New work suggests that chromosome isolation in MN can cause long-lasting alterations in chromatin state and gene expression. Analysis of DNA compaction and histone modifications in MN isolated from cultured cells found that DNA in intact MN is overcompacted and has increased levels of heterochromatin-associated histone modifications [40,41]. These changes were correlated with reduced recruitment of a broad range of histone modifying enzymes to MN, which may reflect defects in protein import or chromatin decompaction [41]. MN chromatin undergoes additional modifications after rupture. Cytoplasmic exposure results in global loss of histone acetylation and further increases H3K9me2 and H3K27me3 marks [40,41]. The rapid deacetylation of MN histones after rupture has led to its use as a sensitive reporter for MN rupture in several systems [26,42]. Alterations to histone modifications can also influence the frequency of MN formation, suggesting that chromatin structure is influential at many points in the MN life cycle [43,44]. Determining the molecular mechanisms driving histone modification alterations in intact MN will be key in understanding how micronucleation defines chromatin structure.

Identification of MDC1 (mediator of DNA damage checkpoint 1) as a persistent marker of damaged chromatin from MN allowed researchers to demonstrate that changes in chromatin organization persist on the MN body, the MNated chromatin, when it is reincorporated into a nucleus [40]. These changes include increased H3K9me2/3 and H3K27me3, which mark constitutive and facultative heterochromatin, and decreased H3K27ac, a euchromatin-associated mark, compared to the surrounding chromatin [40,41]. Further analysis of cell lines allowed to expand after a single MN event suggests that micronucleation could have long-lasting consequences on chromatin structure [40,41]. This long-term alteration of MN chromatin may be under selection to offset the negative consequences of aneuploidy, as MN frequently co-occur with or cause aneuploidy.

Persistent changes in histone modifications may also impact DNA damage repair efficiency and transcription on micronucleated chromatin. H3K36me3 methylation, which participates in the DNA damage response, is enriched in intact MN, though it is not known whether this is sufficient to alter pathway function [41]. Several histone acetylation marks lost on ruptured MN, including H3K27ac and H3K9ac, are necessary for transcription initiation and may contribute to transcription defects in MN [40,41]. In addition, specific histone methylation can promote cGAS binding, suggesting a new potential mechanism influencing MN activation of innate immune signaling [37].

These studies strongly suggest that missegregation into MN is sufficient to disrupt chromatin function for multiple cell cycles, but the consequence of these changes is unclear. To untangle questions about which effects of MN directly affect cellular changes, we recently developed an approach using on-demand automated image analysis and photoactivation to isolate cells with intact and/or ruptured MN from a larger population. Initial results suggest that micronucleation and rupture have little effect on cell transcription compared to the aneuploidy response in the first cell cycle [45], consistent with previous results [46,47]. Continued analysis of these cells over time, however, will be critical to define the impact changes in MN histone modifications have on other cellular processes and on the formation and maintenance of highly rearranged and mutated chromosomes within the population.

Transcription

The extent of transcription loss in intact MN has been unclear, but many studies suggested that there was a strong defect in mRNA production even before MN rupture. Earlier RNA FISH experiments in cultured cells suggested that most intact MN could synthesize mRNA [16]. However, a new study using a bioinformatics approach to estimate MN contribution to cellular mRNA found that over 70% of intact MN were transcriptionally silent, and that this correlated with reduced recruitment of core transcriptional components Cdk12 and Cdk9 [40]. Reductions in active RNA Pol2 in MN have also been observed in many systems [16,40,48]. Altered chromatin compaction, histone modifications, and DNA methylation, though this has not been well characterized in MN, could also contribute to decreased transcription rates. Impaired transcription can persist into the next cell cycle, though specifically on damaged chromatin, suggesting an interdependence between DNA damage and transcriptional silencing [40].

Transcription defects in MN alter gene expression and may also be a major driver of DNA damage through the formation of R-loops. These RNA-DNA hybrids are enriched in MN, either due to the increased errors in transcription or impaired recruitment of R-loop resolving enzymes MPG and APE1, members of the base excision repair pathway. Unrepaired DNA nicks at R-loops can lead to dsDNA breaks upon MN rupture [23]. Overall, the mechanisms behind transcriptional silencing and whether gene expression loss in intact MN is detrimental or protective for the cell, which likely depends on whether the MN chromosome contributes to aneuploidy, are still unknown.

Replication

Intact MN initiate DNA replication, but frequently show delays or defects that can lead to aneuploidy and DNA damage. Estimates of replication timing and extent vary between experiments and cell types, but studies generally find that a significant proportion of intact MN are still replicating in G2 and as the cell enters mitosis [16,18,24,49,50]. Analysis of replication factors identified defects in recruitment of ORC complexes to MN that could underlie these delays [17,50]. This under-replication can be exploited to identify micronucleated chromosomes in subsequent cell cycles and has enabled key insights into the consequences of micronucleation [29]. DNA replication delays in MN may cause DNA damage through multiple mechanisms. Open replication forks are proposed to be a major source of dsDNA breaks during MN rupture and under-replicated DNA activates an error prone replication process in mitosis that generates DNA damage [24,29,51]. Of interest will be whether MN chromatin has continued DNA replication issues in the next cell cycle, similar to what is found for chromatin structure and transcription.

Kinetochore assembly

Chromosomes contained in MN frequently missegregate again in the following mitosis, and this has been connected to defects in chromatin compaction and kinetochore assembly. Analysis of centromere and kinetochore protein recruitment in RPE-1 cell MN found a significant reduction in multiple essential centromeric markers during early interphase, including CENPC, CENPT, CENPA, and H4K20me1 [52]. Work in Ptk1 cell MN, which rarely rupture, found similar results [53], suggesting that these changes likely occur in intact MN. These changes lead to defects in spindle assembly checkpoint activation and substantial rates of re-micronucleation [52,53], supporting a role in MN persistence. Interestingly, an initial analysis of MN fate in cancer cells found that the majority of MN segregated into a main nucleus at the end of the next mitosis [16], suggesting that different cell types may regulate kinetochore assembly differently, or that other spindle characteristics may promote proper MN segregation. Proper histone modification is a key factor in centromere assembly, thus defects in histone modifying enzyme recruitment to MN could be an important mechanism. Overall, a comprehensive analysis of centromere and kinetochore protein recruitment to MN in multiple cell lines will be critical to understand this phenotype.

Nuclear transport defects in micronuclei: a mechanism driving functional change

Although most MN assemble functional NPCs, defects in nuclear import are thought to drive many of the chromatin structure and nuclear function defects observed in intact MN. Analysis of whole chromosome MN indicates that even those containing the smallest human chromosomes form NPCs and can import reporter proteins [42]. However, NPC recruitment or insertion is reduced in most MN, leading to lower NPC densities in multiple systems [16,17,42,48,50,54]. Models of NPC transport in the nucleus suggest that decreased NPC density could significantly slow passive diffusion of small proteins, such as Cdk9 and Cdk12, into the MN [55–57]. Delayed or reduced facilitated import has been observed for several fluorescent reporters in MN, supporting a defect in active MN transport [17,52], although the mechanism is unclear. Interestingly, many of the proteins depleted from MN, including the replication proteins MCM2, MCM3, RNA Pol II (RPB1) [16,40,48,50], the histone ubiquitination complex (RNF40) [41], and the centromere protein CENPC [52], are very large and likely highly sensitive to decreased import efficiency, such as from reduction of the Ran gradient or transport factor availability [58–60].

A defining factor of MN is their presence in the same cytoplasm as the larger main nucleus, which could lead to competition for transport factors and nuclear proteins [61]. Delays in initiating MN import post-mitosis could impair the ability of MN to compete with the nucleus for critical NE proteins during mitotic exit, including chromatin decompaction and nuclear lamina assembly factors [62], and decreases in transport rates could sustain these losses in interphase. Although other MN characteristics, including membrane curvature (lamin B1 [63]) and chromatin state (histone modifiers), also contribute to altered protein recruitment or retention in MN, impaired transport is likely a major factor driving changes in MN composition and function. Further analysis of MN recruitment of major transport factors as well as localization of essential nuclear proteins requiring unique importers, including the proteosome [64] and nuclear actin [65], may yield new insights into the molecular mechanisms of transport defects and how they lead to functional defects in MN.

Chromatin content determines micronucleus structure and function

Chromosome missegregation and micronucleation are determined by both chromosome and spindle characteristics and are often highly biased (Fig. 1.2). New technologies to induce and analyze aneuploidies at the single cell level have shown that delaying cells in prometa- or metaphase in cultured human cells can result in increased missegregation of long chromosomes due to an increased susceptibility to cohesion fatigue [66]. A larger kinetochore region can also increase missegregation after mitotic delay due to increased merotelic microtubule attachments [67]. In contrast, accelerating metaphase by inhibiting the spindle assembly checkpoint (SAC) causes both increased missegregation of large chromosomes, through decreased microtubule error correction at edge of the metaphase plate [68], and increased missegregation of small chromosomes, through an unknown mechanism [66]. Meanwhile, reduced expression of centromere components mainly causes missegregation of chromosomes with small centromeres [69].

Chromosome and spindle characteristics also determine the likelihood of micronucleation after missegregation. Although global mechanisms act to prevent micronucleation [9,70], large chromosomes positioned at the edge of the metaphase plate [68] or chromosomes that are misaligned but satisfy the SAC [6] are more likely to form MN. How other types of mitotic or genetic changes, including aneuploidy, p53 loss, or changes in ER organization, affect micronucleation bias remain to be elucidated.

The biased missegregation of chromosomes into MN has significant implications for interpreting functional defects in MN. Chromosome content can affect the fate of the micronucleated cell in several ways. First, MN containing large or multiple chromosomes recruit more key NE proteins, including NPCs and lamin B1, which delays their rupture [42]. In addition, small chromosomes with low heterochromatin density are able to suppress nuclear lamina gap formation in MN through an unknown mechanism, also delaying rupture [42]. These differences in rupture timing could have significant effects on the type and extent of DNA damage and cGAS activation [30,38]. The mechanism of MN formation can also affect the apparent functionality of MN. Metaphase delay results in MN containing larger and more gene-dense chromosomes that recruit more proteins, have a higher transcription potential, and an earlier replication timing. In contrast, inhibiting the SAC results in more small MN with a wide variation in NE structure defects and baseline transcription. Thus, controlling for changes in MN content will be key to defining mechanisms responsible for MN function defects and membrane rupture.

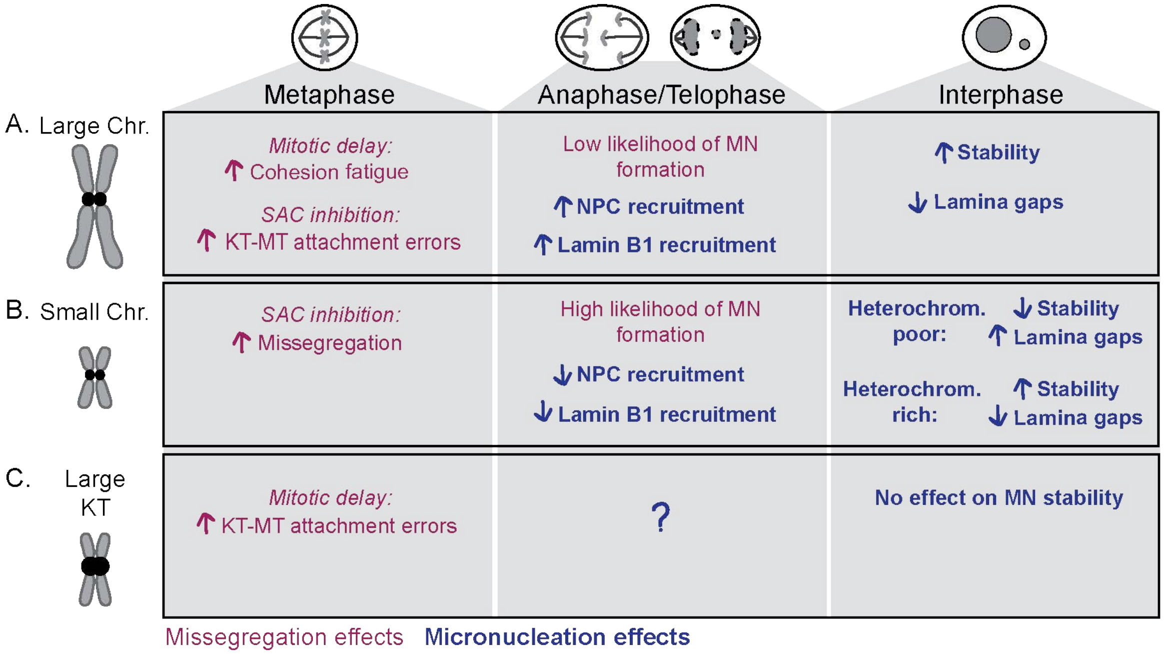

	Metaphase	Anaphase/Telophase	Interphase
A. Large Chr.	*Mitotic delay:* ↑ Cohesion fatigue *SAC inhibition:* ↑ KT-MT attachment errors	Low likelihood of MN formation **↑ NPC recruitment** **↑ Lamin B1 recruitment**	**↑ Stability** **↓ Lamina gaps**
B. Small Chr.	*SAC inhibition:* ↑ Missegregation	High likelihood of MN formation **↓ NPC recruitment** **↓ Lamin B1 recruitment**	**Heterochrom. poor: ↓ Stability ↑ Lamina gaps** **Heterochrom. rich: ↑ Stability ↓ Lamina gaps**
C. Large KT	*Mitotic delay:* ↑ KT-MT attachment errors	?	**No effect on MN stability**

Missegregation effects **Micronucleation effects**

Figure 1.2: The influence of chromosome features on missegregation and micronucleation.

A. Large chromosomes are located at the edge of the metaphase plate leading to missegregation due to an increase in erroneous microtubule (MT)-kinetochore (KT) attachments during SAC inhibition. Large chromosomes also missegregate from susceptibility to cohesion fatigue during mitotic delay. Only a small fraction of large missegregating chromosomes become MN. Large chromosomes recruit higher levels of NE proteins and in MN, delay MN rupture, and form an intact lamina. **B.** Small chromosomes missegregate frequently after disruptions to the SAC. Bypassing the SAC can lead to a higher proportion of missegregating chromosomes becoming MN. Smaller chromosomes recruit lower levels of NE proteins. In MN small chromosome stability is influenced by gene density, with gene rich chromosomes delaying rupture and having fewer defects in their lamina while gene poor chromosomes rupture frequently and contain many lamina gaps. **C.** Chromosomes with large KTs form more KT-MT attachments and have more KT-MT errors during mitotic delay. KT size has no correlation with MN stability.

Concluding remarks and perspectives:

The breadth of research assessing MN function and consequences in recent years has shifted our understanding of MN from outputs of genetic instability to detrimental nuclear compartments that drive further genetic instability. Work characterizing nuclear defects in intact MN suggests that the nuclear environment of MN is highly abnormal and that MN formation in a cell, even prior to rupture, is more disruptive than previously appreciated. Intact MN have defects in all the major nuclear processes studied thus far, which may underlie the massive DNA damage and gene expression changes that follow MN formation. Key questions going forward are: what is the extent of MN functional defects, what is driving them, and which cause persistent changes in the cell? Comprehensive studies of MN protein and RNA content will be critical to identify additional defects; a recent analysis of the MN proteome suggests that the defects reviewed here represent the tip of the iceberg [71]. Whether other nuclear processes, such as the formation of nuclear subcompartments like nucleoli [72], occur efficiently in MN also remains to be determined. Continued analyses of MN transport and chromosome biases will also be key areas of research to understand the fundamental conditions leading to impaired nuclear environments in MN. In addition, global changes in MN chromatin structure suggest alternative mechanisms for the high frequency of nuclear lamina and membrane rupture in MN. For instance, overcompaction may disrupt chromatin interactions with the nuclear lamina, leading to decreased mechanical resistance [73]. Micronucleation biases may also inform the contribution of MN to cancer-specific aneuploidies and chromothripsis events, such as the frequent chromothripsis of chromosome 11 in ependymomas [74], and how well specific micronuclei are tolerated by the cell. Thus, expanding our understanding of the general and specific consequences that encapsulating different chromatin types in MN has on the nuclear environment could define the mechanisms underlying multiple critical steps in the MN lifecycle and the contribution of MN formation and rupture to cell dysfunction. Identifying how this dysfunction varies in different cellular contexts, such as the unique cellular environments of aging or neurological diseases where the impact of MN is not well understood, will help us understand the functional ability of MN in vivo and the contribution they make to disease.

Thesis overview

Overall, the goal of this thesis is to determine how chromosome identity influences the formation, function, and stability of micronuclei so we can better understand the causes and consequences of MN rupture in cancer. Chapter 2 will identify heterochromatin as a key regulator of small MN stability that influences lamina organization and MN growth. While characterizing growth in MN, a defect in MN export is characterized and found to promote MN rupture. Chapter 3 will look at how chromosome identify influences MN formation by assaying MN content after different MN inducing treatments. Finally, Chapter 4 will discuss the implications of these studies and areas of future investigation.

Chapter 2 : Nuclear transport drives micronucleus disruption

Abstract

Micronuclei (MN) form when missegregated chromosomes recruit their own nuclear envelope and are commonly used as a marker of chromosome instability. MN frequently rupture, which causes genome instability, upregulation of metastatic genes, and increased immune signaling. MN rupture is often caused by NE defects, but the cause of these defects is not understood. Previous work from our lab found that chromosome identity regulates the timing of rupture of small MN, MN containing short chromosomes, and that MN with euchromatic chromosomes are more stable due to fewer nuclear lamina defects. Here we find that histone methylation plays an important role in small MN stability and promotes instability through lamina defects and MN growth. Surprisingly, we find all MN to have a severe nuclear export defect that promotes growth and MN rupture. Growth in MN is correlated with the appearance and growth of gaps in the lamina. We find that export defects are correlated with decreased RCC1 levels in MN and that additional loss of RCC1 caused by decreased histone methylation in euchromatic MN results in an additional import and growth defect that prevents nuclear lamina gap growth and membrane rupture. Analysis of mutational signatures associated with early and late rupturing chromosomes in the Pan-Cancer Analysis of Whole Genomes Consortium dataset identified an enrichment of APOBEC signatures on chromothripsis events, suggesting that MN rupture timing is a key determinant of genome evolution in these events. Our study defines a new model of MN rupture where MN growth, driven by defects in protein export, drives defects in nuclear lamina organization that make the MN susceptible to membrane rupture with long-lasting effects on genome architecture.

Introduction

Micronuclei (MN) form when missegregated chromatin recruits its own nuclear envelope during mitotic exit. MN can contain chromatin fragments or one or a few whole chromosomes. MN have been used as markers of exposure to carcinogens, are frequent in many tumors, and occur at elevated rates in genetic diseases, including auto-immune disorders and laminopathies [10,22]. Similar to nuclei, the MN nuclear envelope compartmentalizes chromatin from the cytoplasm, however many nuclear functions are defective in MN including chromatin modifications, transcription, replication, and nuclear transport [75]. Because of these defects MN can lead to functional aneuploidy, where a chromosome is diploid but one copy is not expressed, and DNA damage can occur from erroneous transcription and replication [23,24]. MN are extremely unstable, at least 50% of MN lose compartmentalization in cultured cells by unrepaired rupture of the membrane during interphase and the proportion increases with increasing interphase duration [16]. This chromatin is under replicated and experiences massive DNA damage, driving aneuploidy, and extensive highly localized genome changes, including chromothripsis and kataegis [76]. MN rupture also activates the cGAS-STING innate immune pathway, which can trigger cancer-associated invasion and inflammatory pathways [32,33,77].

The current model for why MN rupture is centered on defects in NE assembly, including decreased density of NPCs and gaps in the nuclear lamina [16]. Small MN containing shorter chromosomes fail to recruit many NE proteins during mitotic exit, especially the “non-core” group of B type lamins, NPCs, and LBR, [17,42]. These defects have been linked to microtubule density or altered AurB activity in the spindle midzone [9,17,70,78]. An alternative model suggests that high curvature inhibits lamin B meshwork formation [63,79]. Defects in NPC recruitment have been suggested to cause the reduction in lamin B1 levels and MN functional defects due to impaired import of replication, transcription, and histone modification proteins [40,41]. However, other studies have found that active import is not regulated by NPC density [59], suggesting that other transport factors are likely disrupted in MN.

We found that MN with high euchromatin have improved nuclear lamina organization despite limited recruitment of lamin B1 and NPCs [42]. This was surprising since chromosomes enriched in euchromatin typically have limited contact with the nuclear lamina and provide less resistance to mechanical force [73,80,81]. However, in MN it is possible the lack of contact between euchromatin and the lamina prevents it from interfering with lamina organization. In addition, MN have a global decrease in histone acetylation and enrichment of histone methylation marks accompanied by decreased transcription, suggesting that euchromatin should be more similar to heterochromatin in MN [40,41]. Therefore, the mechanism by which euchromatin increases MN stability is unclear.

In this study we determine how chromatin state regulates MN stability and identify nuclear export defects as a major driver of NE disruption in MN. We link defects in export to increased nuclear lamina gaps driven by unregulated MN growth. The growth and export defects are linked to specific loss of the RanGEF RCC1, which is required to maintain the Ran gradient [82]. RCC1 is further depleted from euchromatic MN due to the depletion of histone methylation, suggesting a mechanism by which these MN are protected from lamina disruption by additional defects in import, limiting MN growth. In addition, by analysis of cancer genome datasets we find that the early rupture of heterochromatic MN is associated with specific mutational signatures within chromothripsis, demonstrating that MN rupture timing can have long-lasting impacts on genome structure that could alter cancer progression and therapeutic efficacy.

Results

Histone modifications are a key feature for determining small MN stability

In a previous study we identified chromosome identity an important contributor to MN stability, with gene density influencing rupture timing [42] (Fig. 2.1a). Unstable MN rupture early in the cell cycle following their formation from mitotic errors, in G1, while stable MN are able to delay rupture but do eventually rupture later in the cell cycle after DNA replication has been in initiated in S or G2 phase. Large chromosomes form large MN that recruit Lamin B1, NPCs, and are stable. Small chromosomes form small MN, which fail to recruit lamin B1 and vary in stability. Small MN stability correlates with gene density as small, gene poor MN have gaps in their lamina meshwork and rupture early in G1 while small, gene rich MN have an intact lamina and are stable until the G2 phase. For small MN, we still need to know how gene density influences lamina structure and MN stability.

To address this question, we decided to analyze small MN containing a single copy of chr18 or chr19 as models. We chose to use these two chromosomes because they have divergent gene density values and stability in MN, with chr19 being gene rich and very stable, despite being similar in size and NE composition. To understand how gene density influences MN stability, we characterized histone modification levels and active transcription for these chromosomes in MN. We induced micronuclei in non-transformed RPE-1 cells by first synchronizing cells in G1 with a cdk4/6 inhibitor and then releasing cells into a MPS1 inhibitor to disrupt mitosis and increase micronuclei formation. We then fixed cells in following the G1/S phase for immunofluorescence (IF). To identify MN containing a specific chromosome we performed DNA-FISH combined with IF for a centromere marker, to ensure a single chromosome was in each MN, and with a rupture marker (H3K27Ac or LBR) [42] (Fig. S2.1a,b,c). We then quantified H3K27me3 and H3K9me2 (heterochromatin), H3K27ac (euchromatin), and active Pol2 pSer2 (transcription) in intact MN by IF. Analysis of bulk MN recapitulated previous results [40,41], identifying overall higher levels of histone methylation and lower levels of active Pol2 pSer2 (Fig. S2.1d-g). Comparing chr18 and 19 we found chr18 has slightly higher levels of the constitutive heterochromatin marker H3K27me3 compared to chr19, as expected based on gene density and main nucleus data, though similar levels of an additional constitutive heterochromatin marker H3K9me2 (Fig. 2.1b,c). When looking at H3K27ac we found that chr18 and chr19 have similar levels of this euchromatin marker (Fig. 2.1d). We found that both chromosomes had very low levels of active Pol2, suggesting little to no active transcription in these MN, in line with previous studies [40] (Fig. 2.1e). Together this shows that in micronuclei chr18 is slightly more heterochromatic, with more methylation compared to chr19, though the differences are not a large as expected possibly due to global changes in chromatin structure in MN. These results suggest histone modifications as a possible difference between euchromatic and heterochromatic chromosomes in MN that could determine stability.

To test this hypothesis, we altered chromatin and transcription with small molecule drugs and measured the effect on chr18 and 19 MN stability. To alter histone modifications we used methylstat a histone demethylase inhibitor that increases histone methylation making chromatin more heterochromatic and TSA a HDAC inhibitor that increases histone acetylation and makes chromatin more euchromatic. To target transcription we used DRB a transcription elongation inhibitor. To eliminate possible effects on chromosome missegregation frequency or position, these drugs were added after mitosis for 4 hours prior to fixation. For methylstat and DRB we used H3K27ac as a rupture marker and for TSA treatment, because we are inhibiting HDACs, we used LBR as a rupture marker [26,42] (Fig. S2.1c). These treatments were sufficient to alter histone modifications or transcription in nuclei, bulk MN, and chr18 and 19 MN, as expected (Fig. S2.1d-g, Fig. 2.1f-g). Increasing histone methylation with methylstat had a small effect on bulk MN stability, but significantly decreased the stability of chr19 MN (Fig. 2.1h, Fig. S2.1h). Increasing histone acetylation with TSA treatment led to an increase in bulk micronuclei stability as well as increasing chr18 MN stability and slightly increasing chr19 MN stability (Fig. 2.1i, Fig. S2.1i). DRB also affected both chr18 and 19 similarly, leading to a slight decrease in stability, but had not effect on bulk MN (Fig. S2.1h,j). Overall, our results suggest that increasing histone methylation specifically decreases the stability of lmnb1- MN, with larger effects on more euchromatic chromosomes, suggesting heterochromatin as a contributor to small MN instability. In addition, our data suggest that TSA and DRB have more global effects on MN stability, potentially due to additional transcriptional changes in the main nucleus from these drug treatments.

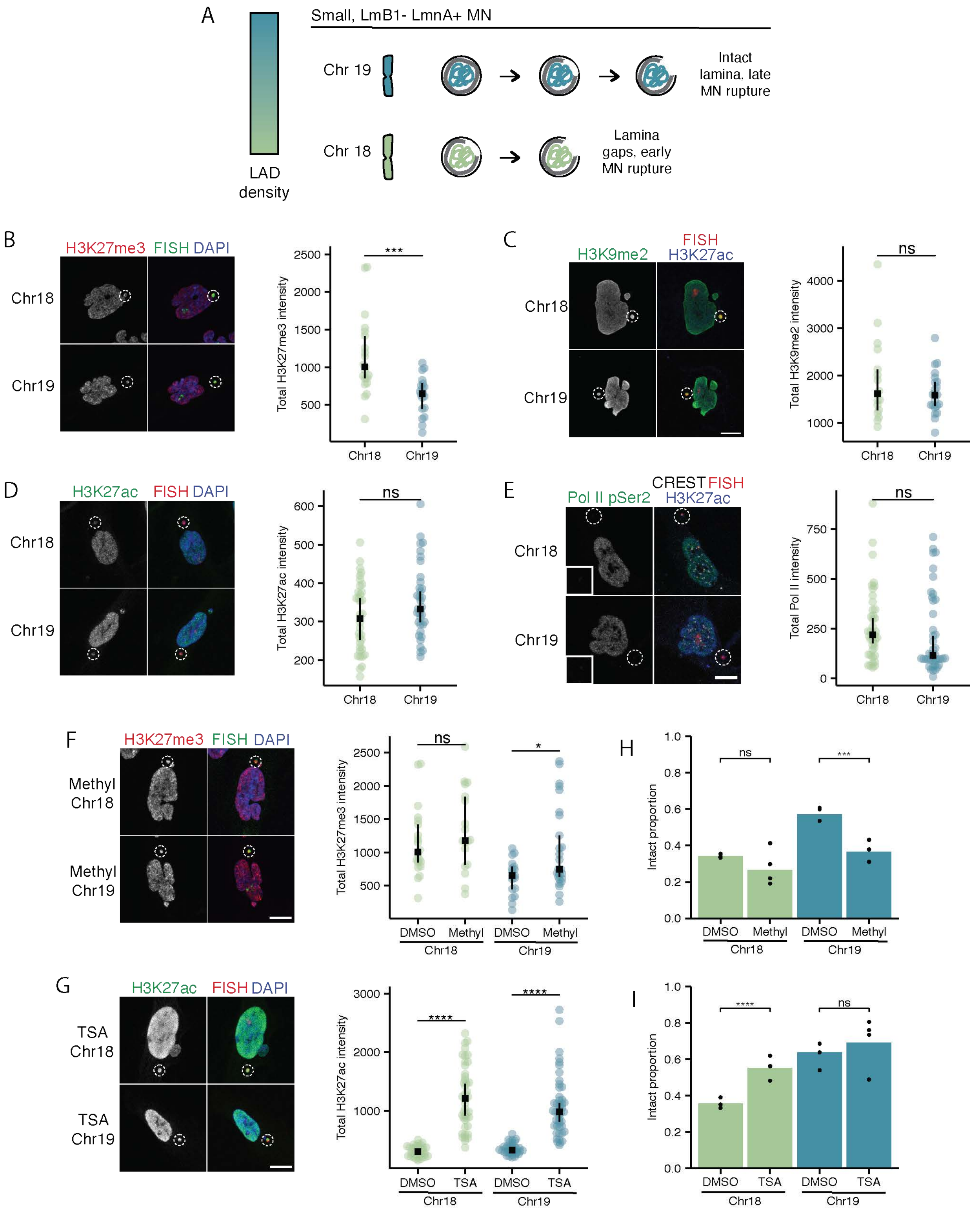

Figure 2.1: Histone modifications regulate small MN stability

A. Summary of the influence of chromosome size and gene density on lamina gap formation and MN rupture timing (Mammel et al). **B-E.** Maximum intensity projections of H3K27me3 (B), H3K9me2 (C), H3K27ac (D), and active Pol2 pSer2 (E) in intact single chromosome chr18 and

19 MN in RPE-1 cells 24hrs post BAY addition. Quantification H3K27me3, H3K9me2, H3K27ac, and active Pol2 pSer2 from sum projections to measure total intensity. Wilcox ran sum test, N=3, H3K9me2 n=(17,22), H3K27me3 n=(21,19), H3K27ac n=(74,65), and pol n=(16, 15) **F.** Maximum intensity projections of H3K27me3 in intact single chromosome chr18 and 19 MN in RPE-1 cells after 4hr treatment with 5uM methylstat. Quantification H3K27me3 from sum projections to measure total intensity. Wilcoxon rank sum test, N=3, n=(21, 18, 19, 26) **G.** Maximum intensity projections of H3K27ac in intact single chromosome chr18 and 19 MN in RPE-1 cells after 4hr treatment with 100nM TSA. Scale bars=10um. Quantification H3K27ac from sum projections to measure total intensity. Wilcox ran sum test, N=3, n=(74,65,90,53) **H.** MN stability for 24hr post BAY release single chromosomes chr18 and 19 MN after 4hr DMSO or 5uM methylstat treatment. Barnards test, N=(4,4,3,3), n=(216,338,165,199). **I.** MN stability for 24hr post BAY release single chromosomes chr18 and 19 MN after 4hr DMSO or 100nM TSA treatment. Barnards test, N=(3,3,4,4), n=(213, 188, 203,112). Scale bars = 10um. For all graphs, ns p>0.05, * p<0.05, ** p<0.01, *** p<0.001, **** p<0.0001. For all dotplots in the article median of all replicates (black square) is shown with 95% confidence interval (black line) and individual measurements (colored circles). For all bar graphs in the article, individual experiments are represented as points and pooled replicate proportions are represented as bars. For all sample sizes, N = number of experimental replicates, n = total number of objects from all replicates.

MN size and lamina organization are altered by histone modifications and correlated with MN instability

To determine how altered levels of histone methylation could regulate MN rupture timing, we first assessed lamina associated domain (LAD) organization before and after incubation in histone modifying drugs in RPE-1 cells. LADs are critical resistors of mechanical force whose disruption leads to altered nuclear stability and were our first hypothesis for how histone modifications may influence stability in small MN. Surprisingly, we found that chr18 and 19 MN had a similar LAD organization in MN, despite significantly different amounts predicted from their sequence [42,83], and that this organization was unperturbed by methylstat or TSA treatment (Fig. S2.2a,b). These data suggest that MNation alters the expected LAD number of chromatin, possibly due to the forced proximity to the lamina when chromosomes are isolated in MN, and that LADs are not responsible for the instability of MN associated with heterochromatin.

During this analysis, we noticed that methylstat treatment led to consistently larger chr19 MN (Fig. 2.2a), but no change in the bulk MN size (Fig. S2.2c), suggesting that MN growth could determine rupture timing. This hypothesis could also explain differences in lamina organization we previously observed where chr19 MN had significantly fewer lamina gaps than other chr18

MN. Live cell imaging of nuclear lamina organization in U2OS cell MN found a strong correlation between increasing MN size and increasing lamina gap size (Fig. 2.2b). In addition, analysis of MN volume and nuclear lamina gap number found that MN containing lamina gaps were larger than those with gaps across chromosome content (Fig. 2.2c). Although we cannot definitively say that MN growth can initiate new lamina gaps, these data strongly suggest that their appearance requires MN growth. We therefore asked whether increasing histone methylation triggered appearance of lamina gaps in addition to an increase in MN size. We found that methystat increased the frequency of nuclear lamina gaps in chr19 MN (Fig. 2.2d,e), consistent with increased size. Conversely, increasing histone acetylation reduced lamina gaps in chr18 MN (Fig. 2.2d,e). Together, these data suggest that histone modifications drive defects in nuclear lamina organization, potentially through MN growth, that are required for MN rupture.

To directly test the effect of MN growth on rupture, we first forced micronuclear growth in RPE-1 cells expressing RFP-NLS using hypotonic treatment, which leads to nuclear swelling within 30 minutes (Fig. S2.2d). We added hypotonic treatment for 1 hour, then added back normal media for 1 hour to enable labeling of DNA structures that are altered during swelling. Live cell imaging of RFP-NLS during hypotonic swelling showed massive disruption of MN. We saw nuclear bleb formation in MN and MN rupture within 5 minutes (Fig. 2.2f). Based on fixed cell analysis only ~15% of MN stay intact compared to 40% in untreated cells, confirming that nuclear growth does cause instability in the bulk MN population (Fig. 2.2g). The effect on MN size could not be measured due to the speed of rupture and low number of intact MN after hypotonic treatment. Interestingly, MN do not normally form blebs and MN rupture is not connected to mechanical stress, but the speed of this growth induced rupture is somehow inducing bleb formation in a similar way to force. Both chr18 and 19 MN had a similar disruption after hypotonic swelling, with the intact proportion of both being reduced similar to the bulk population (Fig. S2.2e). These results show that growth is sufficient to induce MN rupture, regardless of chromosome content.

We next asked whether growth was necessary for MN rupture by inhibiting growth through blocking nuclear import. We first tested the efficacy of inhibiting cargo import by adding the importin a/b inhibitor importazole. However, preliminary analyses of MN growth by live-cell imaging in U2OS cells identified a substantial increase in nuclear rupture prior to import inhibition that complicated interpretation of these results. We then inhibited nuclear growth by overexpressing RanT24N [84], a Ran mutant locked in the GDP bound form that disrupts the Ran gradient and decreases nuclear size. Expression was limited to interphase through use of a dox-inducible system to prevent additional changes from disrupting Ran during mitosis. Induction of RanT24N for 16hrs was sufficient to deplete Ran from nuclei and MN (Fig. 2.2h, Fig S2.2f,g), indicative of Ran gradient collapse, and to decrease nuclear size (Fig. 2.2i). Although we did not observe a significant decrease in MN size, possibly because of a slow MN growth rate in MN (Fig. 2.2j), we did observe a significant increase in bulk MN stability, consistent with our hypothesis that growth is required for MN rupture (Fig. 2.2k).

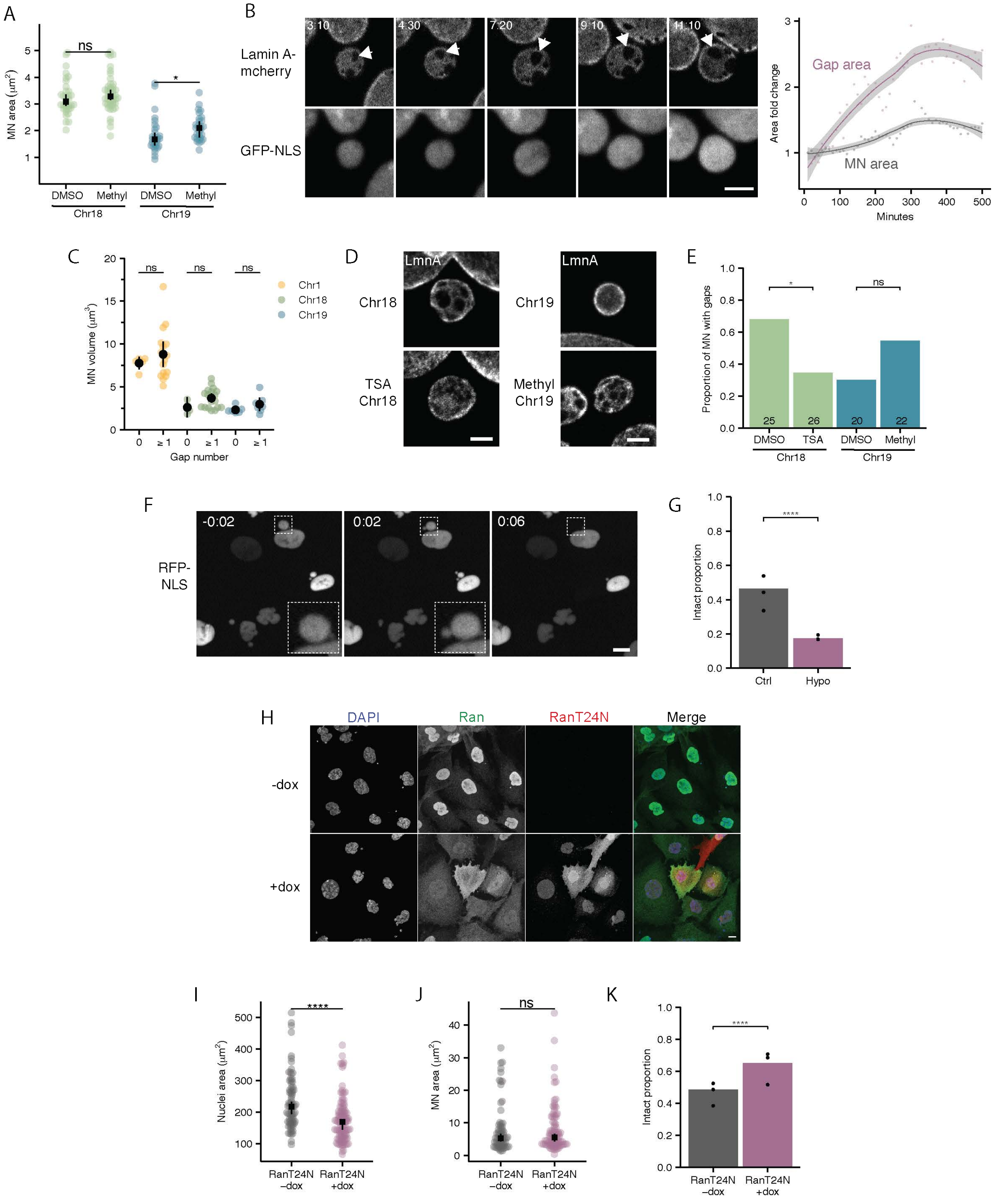

Figure 2.2: MN size correlates with histone modifications and stability

A. Maximum projected area of intact MN 24hrs after BAY for single chromosome 18 and 19 MN in RPE-1 cells. Chr19 MN increase in size after methylstat treatment compared to DMSO.

Wilcoxon ran sum test, N=3, n=(34, 46, 29, 29). **B.** Example of live imaging from U2OS cells expressing Lamin A-mcherry and GFP-NLS imaged every 10 minutes. Single sections shown. Scale bar = 1um. **C.** Comparison of the volume of MN with and with lamina gaps for chr1, chr18, and chr19 MN. Wilcoxon rank sum test, N=3, n=(23, 23, 14). **D.** Max projections of the top surface of intact MN containing single chromosome 18 or 19 MN in RPE-1 cells. Example of MN without gaps for DMSO chr19 and TSA chr19 and example of MN with gaps for DMSO chr18 and methylstat chr19. **E.** Quantification of nuclear lamina organization in MN for each condition. Barnards test, N=3, n=(25, 26, 20, 22). Scale bar = 1um. **F.** Stills from live imaging of RPE-1 cells expressing 2xRFP-NLS and treated with hypotonic media diluted 1:2 in sterile water. Cells were imaged every 2 minutes and timepoints from 2 min before hypotonic treatment, and 2 and 6 minutes after are shown. Inset shows MN undergoing nuclear blebbing and rupture. Scale bar = 10um. **G.** MN stability for bulk intact MN in RPE-1 control and cells and after hypotonic swelling for 1 hour. Barnards test, N= 3, n=(134, 200). **H.** Maximum projection images of RPE-1 TetOn TRE-RanT24N-mcherry cells treated with 0ng/ul and 100ng/ul dox stained for Ran and DAPI showing nuclear expression of mcherry and loss of nuclear Ran with dox addition. Scale bar = 10um. **I,J.** Max projected area of nuclei and intact MN, based on H3K27ac staining, in RPE-1 TetOn TRE-RanT24N-mcherry cells treated with 0gn/ul or 100ng/ul dox for 16hrs. **I.** Nuclei: Wilcoxon rank sum test,. N=3, n=(79,113). **J.** MN: Wilcoxon rank sum test, N=3, n=(72,97). **K.** MN stability in RPE-1 TetOn TRE-RanT24N-mcherry cells treated with 0gn/ul or 100ng/ul dox for 16hrs. Barnards test, N=3, n= (373,487). For all graphs, ns p>0.05, * p<0.05, ** p<0.01, *** p<0.001, **** p<0.0001.

MN overgrow due to a defect in nuclear export

To better define the connection between growth and MN stability, we next asked what determined growth rate and size in MN. Analysis of MN growth by live-cell imaging found a strong defect in initial post-mitotic expansion, consistent with previous observations of increased chromatin compaction [40,41] (Fig. 2.3a). However, unlike nuclei, which obtain a specific nuclear to cytoplasm ratio and stop expanding, MN continued to expand throughout interphase until rupture. This led us to examine the major regulators of nuclear growth in MN. Previous work identified a strong dependence on a nuclear pore protein [85], B-type lamin levels [86], and nuclear transport [87] for nuclear growth. Because MN have reduced densities of NPCs and B-type lamins [42], especially small MN such as those containing chr18 and 19, we focused on assessing differences in nuclear transport in MN.

Previous work identified defects in nuclear import in MN [17,52], but this would not explain the continuous growth we observed. Therefore, we assessed both import and export rates in MN using a small optogenetic reporter, mCherry-LEXY [88]. The LEXY protein contains a weak NLS, a mcherry tag, and a LOV2 domain with an NES that is hidden but uncages with exposure to UV light (Fig. 2.3b). In the absence of UV light the LEXY protein is imported into nuclei as only its weak NLS is accessible. During UV exposure the NES is released and the protein is exported to the cytoplasm due to the strength of the NES compared to the NLS. We expressed NLS-mcherry-LEXY in RPE-1 cells with H2B-miRFP to identify nuclei and MN. Cells were imaged for the 647nm (H2B) and 568nm (LEXY) channels every 30 seconds for 5 minutes to measure starting intensities, imaged for 647nm, 568nm, and 405nm channels at 30 second intervals over 45 min to measure for export, and then imaged again in the absence of UV every 30 seconds for 25 min to measure re-import (Fig. 2.3c,d). To reduce the effect of different volumes of MN and nuclei on analysis of transport rates, we calculated the relative initial import and export rates when permeability difference and volume differences are expected to have negligible effects [59]. To correct for different starting concentrations across cells and compartments, we also calculated the relative effective transport rate for both N and MN [59]. We observed a linear relationship between cargo concentration and transport rate for both MN and nuclei across all concentrations, indicating that expression of LEXY does not saturate the transport machinery [59] (Fig. 2.3g,h).

We obtained a median initial rate of nuclear export of -20.7 AU/s and a median import rate of 8.2 AU/s. Surprisingly, we observed no difference in import rate for MN compared to nuclei in the same cell or across cells after adjusting for cargo concentration (Fig. 2.3e). Instead, we saw a substantial defect in nuclear export with the effect export rate about 2x slower for MN despite a frequently higher starting concentration and a smaller volume that would be expected to reach stead state faster (Fig. 2.3f). These changes were independent of the size of the MN (Fig. S2.3a), indicating that they are not correlated with NPC density. Consistent with this model, MN had higher levels of LEXY at steady state when the NES was exposed compared to nuclei (Fig. S2.3b), as expected if export rates are slower in MN compared to nuclei.

As an additional control, we analyzed the relative nuclear fluorescence of GFP tagged with a strong NES and a strong NLS (NES-GFP-NLS) in nuclei and MN in fixed cells. An export defect would be expected to result in increased steady-state GFP fluorescence in the MN, which is what we observed (Fig. 2.3i). The difference in NES-GFP-NLS accumulation also increased over time, along with MN size, consistent with a growth resulting from a defect in export rather than a defect in DNA decompaction. This result was not limited to RPE1 cells, as a similar accumulation of NES-GFP-NLS was observed in U2OS cell MN (Fig. S2.3d).

Interestingly, we observed that cells expressing LEXY showed a consistent increase in MN versus nucleus mCherry levels prior to uncaging the NES sequence, when only the weak NLS was available (Fig. S2.3b). We observed similar results using a 2xRFP-NLS construct in RPE1 cells (Fig. 2.3j). Steady state levels of NLS or NES reporters are determined by the rate of facilitated transport versus passive diffusion through the pores. Based on the similarities in import rates observed between the two compartments, our data strongly suggest that MN have additional defects in passive transport. Since the rate of passive transport is largely determined by the size of the cargo, we would expect LEXY to show a larger accumulation in MN compared to 2xRFP-NLS, which is what we observe (Fig. S2.3b,g). Both NES-GFP-NLS and RFP-NLS levels are independent of MN size (Fig. S2.3c,e,f).

To test the extent of this export defect in MN we completely inhibited export by incubating cells in leptomycin b (leptB), a CRM1 competitor, for 5 hours. These conditions were sufficient to increase accumulation of GFP-NES and NES-GFP-NLS in nuclei (Fig. S2.3h,i,j) and increase nucleus size (Fig. 2.3k). However, despite an increase of GFP-NES levels in MN (Fig. S2.3j), blocking export with leptB was insufficient to increase bulk MN size or drive changes in MN rupture frequency (Fig. 2.3l,m, Fig. S2.3i), consistent with most MN already having a significant export defect. Overall, our data strongly indicate that MN have a substantial defect in nuclear export, regardless of content or size, and a minimal defect in import of small cargo.

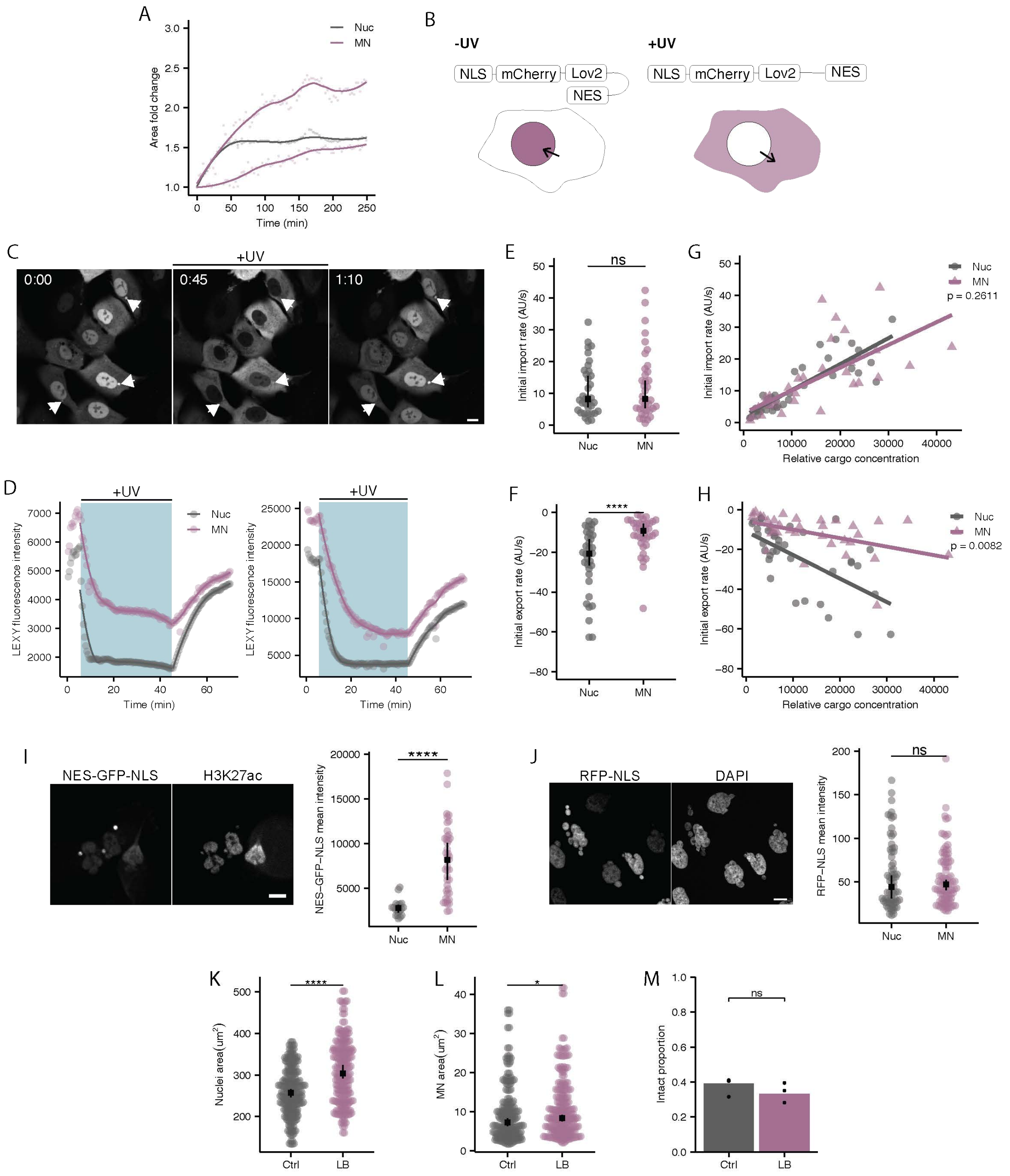

Figure 2.3: MN overgrow due to a defect in nuclear export

A. Nuclear area measurements of U2OS cells expressing GFP-NLS synchronized in G2 with 7.5 um R0-3306, released, and imaged every 3 minutes. Area of nuclei and MN measured from GFP-

NLS channel staring with time 0 at GFP-NLS import after mitosis. **B.** Schematic of NLS-LEXY-mcherry domains. In the absence of UV the NES of LEXY is hidden and the NLS dominates leading to nuclear localization of LEXY. When exposed to UV the NES is exposed leading to export or LEXY form the nucleus. **C.** Image of single sections from live imaging in RPE-1 cells expressing NLS-LEXY-mcherry and H2B-miRFP to identify nuclei and MN during imaging. Cells were images every 5 minutes. Still show cells at the start of imaging without UV, after 45 minutes of UV exposure every 5 minutes, and after 25 minutes in the absence of UV. Scale bar = 10um. **D.** Examples of LEXY intensity quantification in nuclei and MN in RPE-1 cells throughout imaging outlined in C**. E.** Nuclear import rates quantified from LEXY import over 25 minutes in the absence of UV in paired nuclei and MN. Paired Wilcoxon rank sum test, N=3, n=34. **F.** Nuclear export rates quantified from LEXY export during 45 minutes of UV exposure in paired nuclei and MN. Paired Wilcoxon rank sum test, N=3, n=34. **G, H.** Import or export rates compared to the LEXY-mcherry concentration, quantified from cytoplasmic LEXY signal, in RPE-1 cells. Analysis of covariance test. **I.** Maximum projection of RPE-1 cells expressing NES-GFP-NLS. NES-GFP-NLS intensity was quantified for nuclei and intact MN. Wilcoxon rank sum test, N=1, n=(20,43). **J.** Maximum projection of RPE-1 cells expressing RFP-NLS. RFP-NLS intensity was quantified for nuclei and intact MN. Wilcoxon rank sum test, N=3, n=(70, 93). **K, L.** Maximum projected areas were calculated for nuclei and intact nuclei in RPE-1 cells for control and 5hr 20ng/ul leptB treatments. Wilcoxon rank sum test. Nuclei: N= 3, n=(238, 250), MN: N= 3, n=(214, 252). **M.** MN stability in RPE-1 cells for control and 5hr 20ng/ul leptB treatments. Barnards test , N=3, n=(218, 286). For all graphs, ns p>0.05, * p<0.05, ** p<0.01, *** p<0.001, **** p<0.0001.

High euchromatin leads to additional defects in MN import

Transport issues in MN lead to an export defect and accumulation of proteins in the MN nucleoplasm but the extent of transport loss is variable within the population. To determine whether growth is contributing to instability in MN, we first wanted to characterize transport in chr18 and 19 MN to identify where they fall within this range of defects. Since our hypothesis is that transport is responsible for growth and instability in MN, then we would expect chr18 MN to have more active transport than chr19.

We again used NES-GFP-NLS to measure export and import levels and RFP-NLS to measure import and diffusion levels and looked at chr18 and 19 MN specifically. Chr18 MN had similar levels of RFP-NLS to the bulk population while chr19 MN were depleted, suggesting that chr19 MN struggle with import (Fig. 2.4a). Surprisingly NES-GFP-NLS levels are similar in chr18 and 19 MN (Fig 2.4b). Together with the RFP-NLS data, this suggests that chr19 MN are less active than chr18 in import but both have an export defect.

If chr19 MN have a defect in import as well as export, then we expect them to be less affected by leptB treatment. We found that leptB slightly increased the area of chr18 but not chr19 MN (Fig. 2.4c), but similar to the bulk results leptB did not alter MN stability for either chromosome (Fig. 2.4d). This is not due to an inability of chr19 to expand, as both chr18 and 19 MN ruptured at similar frequencies during hypotonic swelling (Fig. S2.2e). Together these data confirm that all MN are defective in export and that chr18 MN have higher transport levels and growth potential than chr19 MN.

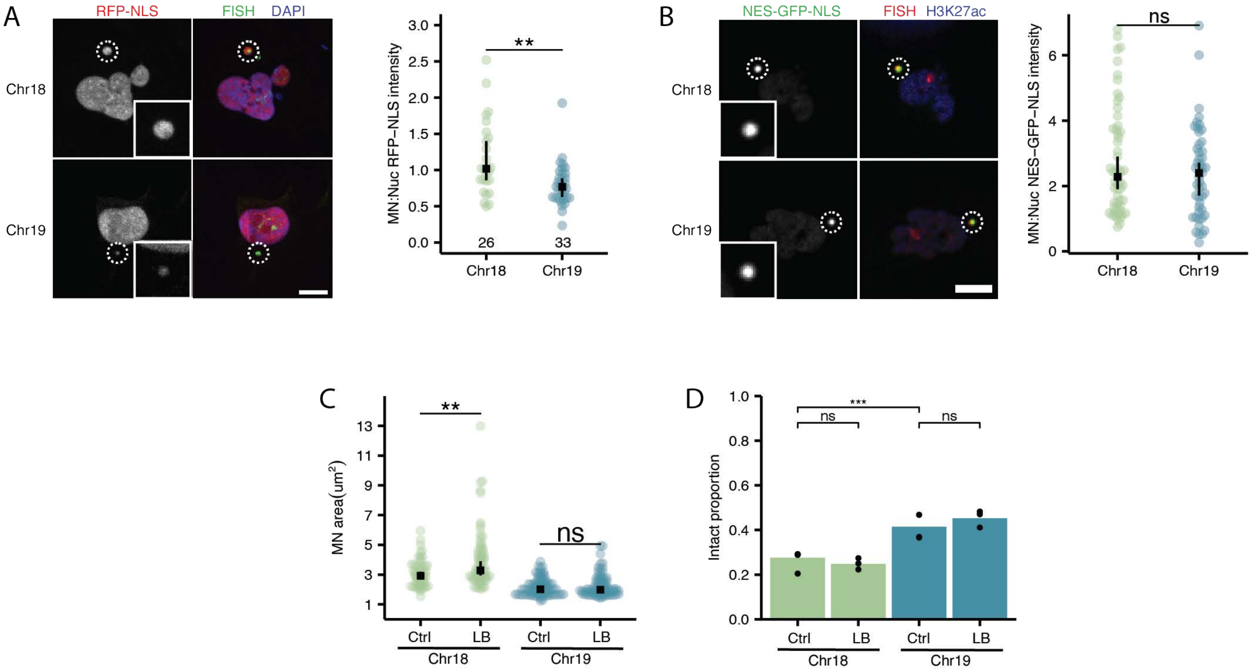

Figure 2.4: High euchromatin leads to additional defects in MN import

A. Maximum projections of intact single chromosome 18 and 19 MN in RPE-1 cells expressing RFP-NLS. RFP-NLS intensity was quantified from single sections for nuclei and intact MN. Wilcoxon rank sum test, N=3, n=(26, 33). **B.** Maximum projections of intact single chromosome 18 and 19 MN in RPE-1 cells expressing NES-GFP-NLS. NES-GFP-NLS intensity was quantified from single sections for nuclei and intact MN. Wilcoxon rank sum test, N=4 , n=(56, 49). **C.** Maximum projected areas for intact single chromosome 18 and 19 MN in RPE-1 cells for control and 5hr 20ng/ul leptb treatments. Wilcoxon rank sum test, N=3, n=(62, 78, 94, 92). **D.** MN stability for single chromosome 18 and 19 MN 24hr post BAY release with 5hr control and 20ng/ul leptB treatments. Barnards test, N=3, n=(261,323,304,243). For all graphs, ns $p>0.05$, * $p<0.05$, ** $p<0.01$, *** $p<0.001$, **** $p<0.0001$.

Defects in RCC1 recruitment result in decreased nuclear export in MN.

Nuclear export rates are dependent on NPC proteins, transportin concentration, and the Ran gradient. To determine the mechanism of MN export defects, we quantified changes in these components in MN compared to nuclei. Consistent with previous results, we found that NPC proteins were generally depleted in MN, correlated with the size of the MN, but neither of the transport rate associated regulators, Nup153 and TPR, nor the protein export receptor, CRM1, were largely reduced below the level expected by the overall reduction in pore number (Fig. S2.4a-c). In contrast, Ran levels were variable across MN and not correlated with MN size, unlike NPC density (Fig. 2.5a, Fig S2.4d). Ran is normally found concentrated at a 3:1 ratio in the nucleus compared to the cytoplasm. In RPE-1 cells we see a Nuc:Cyto ratio of 3.12, as expected, but we find MN have a more variable nuclear Ran concentration and many are depleted (Fig. 2.5a).

RCC1, the RanGEF, is required for Ran accumulation in the nucleus and export is specifically sensitive to changes in RCC1 activity [89]. Therefore, we hypothesized that reduced RCC1 in MN is a major driver of the MN export defect. We observed decreased micronuclear RCC1 levels in both RPE-1 and U2OS cells (Fig. 2.5b, Fig. S2.4f,g). Similar to Ran, RCC1 levels are not correlated with MN size in RPE-1 or U2OS cells (Fig. S2.4e,h). To test the role of RCC1 depletion in defective export in MN we increased RCC1 levels in MN using a fusion gene of RCC1 and H2A to force chromatin association of RCC1. We expressed RCC1-H2A in RPE-1 cells right before release into a Mps1 inhibitor, as cell are entering mitosis and forming MN. RCC1-H2A expressing cells were binned into low and high expressing cells based on RCC1 intensity in the corresponding nucleus. High expression of RCC1 rescued MN stability compared to low expressing and control cells (Fig 2.5c). RCC1-H2A expression also led to a decrease in the accumulation of NES-GFP-NLS in MN (Fig. 2.5d), though NES-GFP-NLS levels in MN with RCC1-H2A are still elevated above nuclear levels likely due to issues with DNA decompaction in

MN [41]. Together, these data support RCC1 depletion as a key contributor to defective nuclear export in MN.

Additional loss of RCC1 in high euchromatin MN causes additional import defects.

Transport levels have been connected to chromatin state, as heterochromatin loss causes a depletion in nuclear Ran concentration, through the enrichment of RCC1 on H3K9me3 and H3K27me3 heterochromatin [90]. To see if heterochromatin influences transport in MN we then looked at Ran and RCC1 levels in chr18 and 19 MN. Ran slightly differs between the chromosomes in MN, with chr19 being more depleted, but both chromosomes are able to form the Ran gradient in MN (Fig. 2.5e). We also found chr19 MN to be especially depleted for RCC1, while chr18 MN had more enrichment but were still lower than nuclei levels, again similar to the bulk population (Fig. 2.5f). RCC1 is known to bind chromatin and is enriched on heterochromatin [90], in line with its depletion from chr19 MN. To test whether heterochromatin levels influence RCC1 recruitment in MN we looked at RCC1 levels on TSA chr18 or methylstat chr19 MN. We saw that methylstat treatment increased RCC1 levels on chr19 MN (Fig. 2.5g), and in the bulk MN population (Fig. S2.4i), while TSA treatment specifically lowered chr18 MN RCC1 levels (Fig. 2.5g). Together these results show that RCC1 is influenced by heterochromatin levels in MN. From this we hypothesize that RCC1 may be responsible for the growth, lamina gaps, and instability in chr18 MN.

To test this hypothesis we altered RCC1 activity in chr18 and 19 MN. To lower RCC1 levels in chr18 MN we used RanT24N, which inhibits RCC1 while blocking import and export. In line with our model, RanT24N expression slightly decreased the presence of lamina gaps in chr18 MN (Fig. 2.5h) and increases the stability of both chr18 and 19 MN (Fig. 2.5i). However, RanT24N did not alter MN size for either chromosome (Fig. 2.5j). It’s possible that these MN are already too small to see a decrease in size, or that stopping all nuclear transport has additional effects on stability that complicate our results.

We next increased RCC1 activity in chr19 MN using RCC1-H2A expression. RCC1-H2A expression did increase RCC1 levels in chr19 MN, though results in a mixed population due to a low nucleofection efficiency (Fig. 2.5k). We saw a slight decrease in chr19 MN stability with the expression of RCC1-H2A (Fig 2.5l). Together these data support RCC1 as potential regulator of small MN stability.

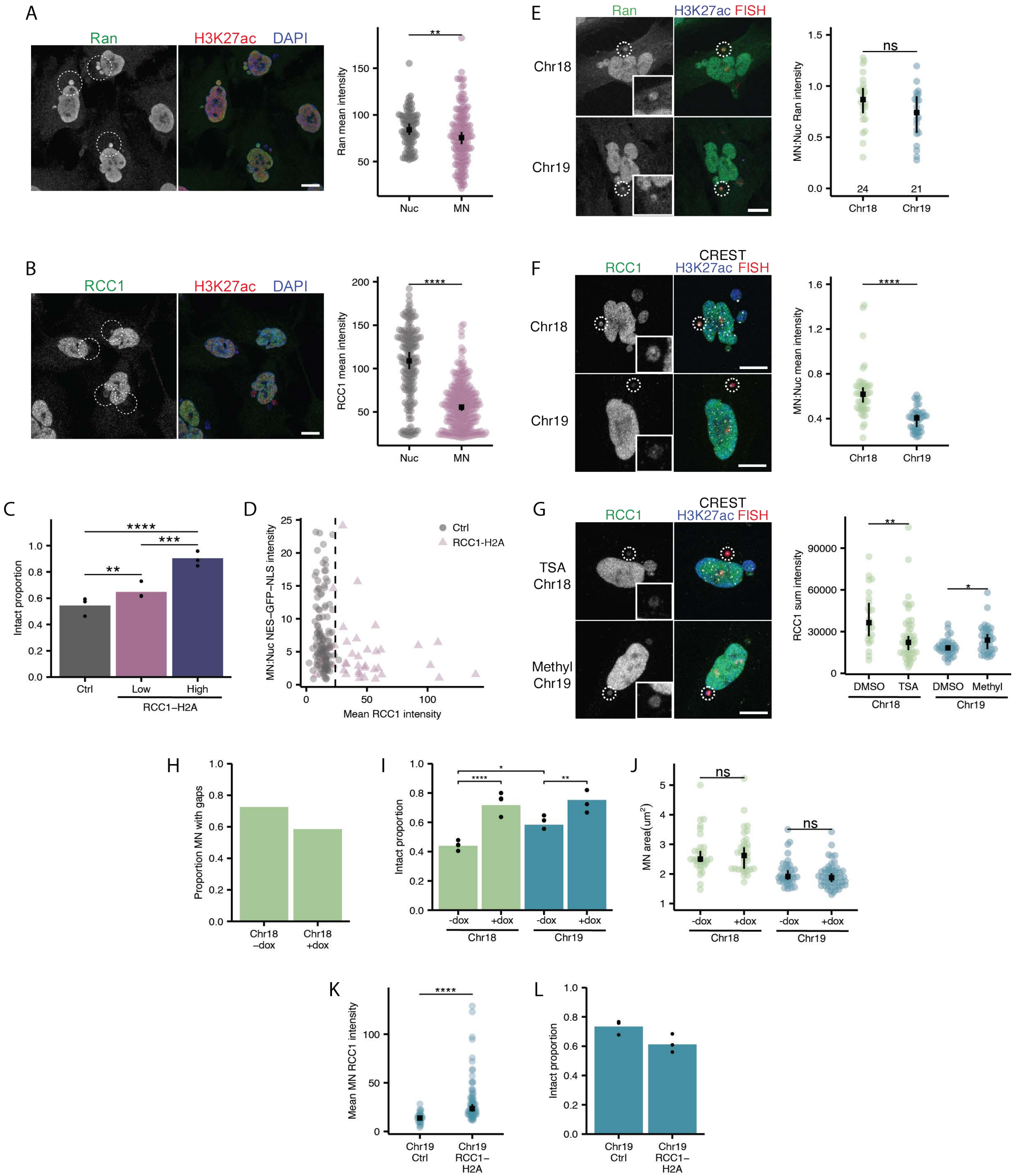

Figure 2.5: Defects in RCC1 recruitment result in decreased nuclear export in MN

A. Maximum projections of Ran in RPE-1 cells 24hrs post BAY addition. Intact MN indicated with white circles. Wilcoxon rank sum test, N=3, n=(88, 140). **B.** Maximum projections of RCC1 in

RPE-1 cells 24hrs post BAY addition. Intact MN indicated with white circles. Wilcoxon rank sum test, N=3, n= (168, 268). **C.** MN stability in RPE-1 cells for after RCC1-H2A expression. Cells in RCC1-H2A samples were binned into high and low intensity groups by eye based on nuclear RCC1 intensity. Barnards test, N=3, n=(294, 349, 73). **D.** For control and RCC1-H2A cells, the comparison between MN:Nuclei mean intensity of NES-GFP-NLS and RCC1 mean intensity for MN in each condition. N=1, n=(272, 82). **E.** Maximum projections of Ran in intact single chromosome 18 and 19 MN in RPE-1 cells 24hrs post BAY addition. Wilcoxon rank sum test, N=3, n=(24, 21). **F.** Maximum projections of RCC1 in intact single chromosome 18 and 19 MN in RPE-1 cells 24hrs post BAY addition. Wilcoxon rank sum test, N= 3, n=(46, 41). **G.** Maximum projections of RCC1 intact single chromosome 18 and 19 MN in RPE-1 cells treated with DMSO, 5um methylstat, or 100nm TSA. Wilcoxon rank sum test, N=3, n=(23, 46, 35, 36). **H.** Quantification of nuclear lamina organization in single chromosome 18 MN 24hr post BAY for RPE-1 RanT24N-mcherry cells treated with 0ng/ul or 100ng/ul dox. N=3, n=(40, 41). **I.** MN stability for single chromosome 18 and 19 MN 24hr post BAY release for RPE-1 RanT24N-mcherry cells + or - dox. Barnards test, N=3, n=(148, 152, 120, 121). **J.** Maximum projected areas of intact chromosome 18 and 19 MN in RPE-1 TetOn TRE-RanT24N-mcherry cells treated with 0 or 100ng/ul dox for 16 hours. Wilcoxon rank sum test, N=3, n=(31,34,36,55) **K.** Quantification of total RCC1 intensity in single chromosome 19 MN 24hr post BAY for control and RCC1-H2A expressing RPE-1 cells. Wilcoxon rank sum test, N=3,4, n=(29,76). **L.** MN stability for single chromosome 19 MN 24hr post BAY in control and RCC1-H2A expressing RPE-1 cells. Barnards test, N=3, n=(116, 82). For all graphs, ns p>0.05, * p<0.05, ** p<0.01, *** p<0.001, **** p<0.0001.

MN rupture timing correlates with chromothripsis DNA damage signature

Previous data shows that chr18 MN rupture early, during G1, while chr19 MN delay rupture until G2 or S phase [42]. MN rupture after DNA replication has been connected to double stranded DNA breaks [16,24,29,50] while rupture in G1 mainly includes the formation of single stranded DNA [26]. Based on these differences, we hypothesized that differences in rupture timing would influence the type of DNA damage that occurs on MN chromatin.

To test this hypothesis, we analyzed data collected from the Pan-Cancer Analysis of Whole Genomes (PCAWG) Consortium, which contains whole genome sequencing data of chromothripsis events from 2,658 tumors across 38 cancer types [91]. To look at rupture timing we divided chromosomes in to 3 categories: early rupturing (chr13, 18, and 21), mid rupture (chr7-12, 14-16, 20, and 22), and late rupturing (chr1-6, 17, 19, X) based on previously identified MN rupture frequencies (Fig. 2.6b) [42]. Chromothripsis events are present on chromosomes in all categories and are not biased by confidence or type of chromothripsis (Fig. S2.6a,b). We identified DNA damage signatures on chromosomes with and without chromothripsis for each rupture timing category (Fig. S2.6c) and looked at whether signatures were enriched in any category.

We found enrichment of APOBEC signatures in chromothripsis events on early rupturing chromosomes in both the presence and severity of mutations (Fig. 2.6c). This enrichment is only seen in chromothripsis events and not in samples with no chromothripsis signatures (Fig. S2.6d). These results are in line with the known mechanisms of DNA damage during G1 as APOBEC mutations are associated with kataegis and ssDNA formation [27,92]. These data show that MN rupture timing can have lasting effects on genome integrity in vivo.

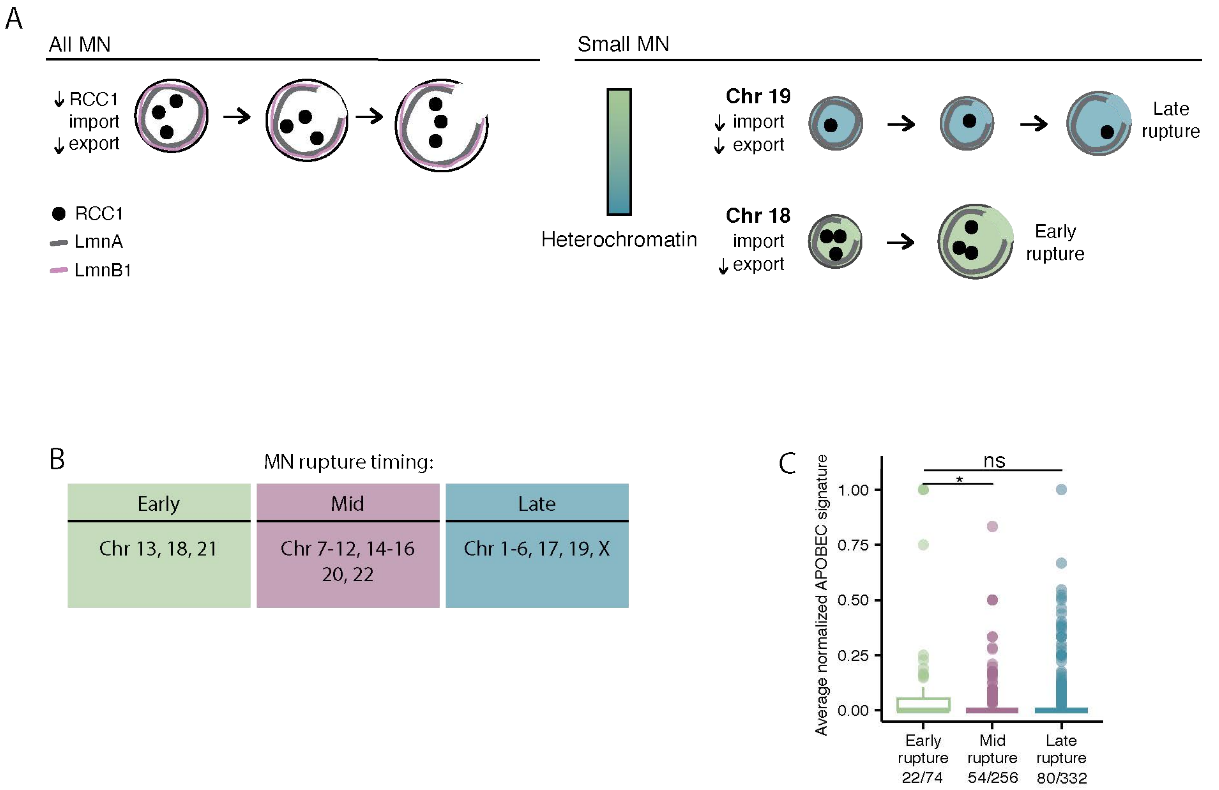

Figure 2.6: APOBEC signatures are enriched in early rupture chromosome chromothripsis events

A. Model of MN rupture due to transport induce growth in all MN, or small MN. **B.** MN rupture timing classification based on chromosome length, LAD density, and previously analyzed rupture frequencies in RPE1 cells (Mammel et al.). **C.** Survey of mutational signatures identifies APOBEC as enriched in high confidence chromothripsis events in early rupture chromosomes. Number of non-zero datapoints out of the total are indicated under each group. Anova, p=0.0166, Tukey honest significant difference test used for pairwise differences. n=(74, 256, 332). For all graphs, ns p>0.05, * p<0.05, ** p<0.01, *** p<0.001, **** p<0.0001.

Discussion

In this study we discover that heterochromatin influences stability in small MN and identify a new pathway contributing to MN rupture: growth though transport. We find that all MN import but have a defect in export leading to an accumulation of nuclear proteins, overgrowth, and lamina gap formation (Fig. 2.6a). Our model suggests that this export defect is caused by RCC1 depletion as other key export factors are not largely lost from MN. We propose that histone methylation levels determine RCC1 recruitment and that euchromatic MN are especially depleted for RCC1, which delays their rupture (Fig. 2.6a). Analysis of existing chromothripsis data shows that early rupturing MN have more APOBEC mutations, supporting a lasting effect of MN rupture timing differences on genome stability.

Chromatin organization leads to instability in MN

Our results find that increasing histone methylation in MN leads to instability while increasing histone acetylation leads to stability. This is in opposition to chromatin's role in nuclear stability, where histone methylation confers stability by increased stiffness [73] and increasing histone acetylation and transcription leads to more nuclear blebbing and instability [80]. Unlike the nucleus, MN rupture is not connected to mechanical force [93] therefore the rigidity of heterochromatin may be detrimental in the absence of force. We do see bleb formation during MN rupture with rapid hypotonic growth, suggesting that the growth can alter internal forces on MN, though more work is needed to fully define this process.

Lamina defects in MN rupture

We see LAD formation in both chr18 and 19 MN despite predicted differences in LAD amount based on their sequence. MN are enriched for histone methylation in general [40,41], so it is surprising that lamina interactions are still sufficient to form nuclear compartments even in a mostly heterochromatic environment. Future work looking at the mechanics of heterochromatin in MN will help determine its role in rupture and lamina interactions. Despite all MN having elevated histone methylation, heterochromatic MN have more lamina organization issues than euchromatic MN, even though heterochromatin normally associates with the lamina. However, these lamina gaps are not sufficient for MN rupture as they are seen in many intact MN, suggesting the need for an additional rupture trigger. Identifying whether transport defects are sufficient for rupture or if they mainly enable additional mechanisms that trigger rupture will be essential to defining the necessity of lamina gaps in MN rupture.

Transport defects regulate MN stability

The continuous growth of MN likely occurs because of their location in the same cytoplasm as a fully functioning nucleus, which constantly replenishes the cytoplasmic cargo from proper nuclear transport. This accumulation of proteins in MN due to defective export may cause accumulation of specific proteins that trigger MN rupture, such as ATR [18] or Chmp7 [19,20]. Also, many of our results suggest competition between nuclei and MN for transport. Competition with the nucleus for cellular proteins, specifically during mitotic exit, may contribute to the timing or frequency of MN rupture. When the Ran gradient is collapsed during RanT24N expression we see a global increase in MN stability, without a change in MN size, that is not fully explained by our model. It is possible that this collapse relieves nuclear competition, which promotes MN stability. Competition with the nucleus is also a potential mechanism by which all MN are depleted for RCC1. Further testing this connection between nuclear compartments will help elucidate how transport defects originate in MN.

The influence of MN rupture timing in cancer

We outline how small, gene rich MN, such as chr19, delay rupture. The stability of small gene rich MN is especially relevant to cancers with double minute chromosomes. Double minutes are amplified copies of oncogenes, commonly containing the Myc gene [94], that are organized into circular DNA that readily forms MN that rarely undergo MN rupture [95]. The mechanism behind small gene rich MN stability we have uncovered here might be applicable in these unique MN and could explain why they are so stable in cancer cells. In addition, we find chromothipsis on early rupturing chromosomes to be enriched for mutational signatures associated with kataegis [92]. This suggests that either rupture before DNA replication or an extended time in the cytoplasm after rupture may influence the acquisition of these hypermutations on MN chromatin. Together, these findings support MN rupture timing as an important factor determining the lasting effects MN formation will have in cancer tissues.

Methods

Cell lines and culture methods

hTERT-RPE-1 (RRID: CVCL_4388) cells were grown in DMEM/F12 (Gibco) + 10% FBS (Gibco) + 1% Pen-Strep (Gibco) + 0.01 mg/ml hygromycin (Sigma-Aldrich) at 5% CO_2 and at 37°C. pLVXE-neo:H2B-emiRFP, pLVXE-Blast:2xRFP-NLS, and pLVXE-Blast:NES-GFP-NLS were introduced by stable transduction into hTERT-RPE-1 cells. pLVX-Neo:Eto.1 (TetOn) was introduced by stable transfection into hTERT-RPE-1 cells followed by stable transfection with pLVXE-Blast:TRE-RanT24N-mcherry. RPE-1 TetON TRE-RanT24N-mcherry cells were grown in DMEM/F12 media with tet-free FBS (GeminiBio). U2OS (ATCC:HTB-96) cells were grown in DMEM (Gibco) + 10% FBS (Gibco) + 1% Pen-Strep (Gibco) at 10% CO_2 and at 37°C. U2OS GFP-NLS Lamin A-mcherry is a stable cell line characterized previously [96].

To induce MN for RPE-1 IF and IF+FISH experiments and U2OS IF experiments cells were arrested in G1 by addition of 1 μM PD-0332991 isethionate (Cdk4/6i; Sigma-Aldrich) for 24 hrs. Cells were released by washing three times in 1× PBS before incubation in 100 nM BAY-1217389 (Mps1i; Thermo Fisher Scientific) for 24 hrs, unless otherwise noted. For drug treatments altering histone modification and transcription with Methylstat (histone demethylase inhibitor; Abcam; ab144566), TSA (HDACi; Cell Signaling; 9950), and DRB (RNA Pol II inhibitor; Sigma; D1916;), RPE-1 cells were treated 5uM methylstat, 100nM TSA, 100ug/mL DRB, or equal volume DMSO for each for 4 hrs before the 24 hrs post BAY timepoint. For lamina gap analysis cells were fixed at 20 hrs post BAY addition. For MN growth and imaging, RO-3306 was used in U2OS GFP-NLS Lamin A-mcherry cells at 7.5 uM for 16.5 hrs and released by washing 7x with warm media before live imaging for MN growth and lamina gap growth.

For hypotonic swelling RPE-1 cells in 100 nM BAY were treated 2 hrs before the 24 hr post BAY timepoint. Media with 100nM BAY was diluted 1:2 in sterile water for 1hr then replaced with normal media with 100nM BAY for 1 hr before fixing cells. RPE-1 tetON TRE-RanT24N-mcherry cells were grown in tet-free media. Cells were treated with 1 uM PD for 24 hrs, 100 nM BAY for 24 hrs. 100 ng/ul doxycycline (Clontech) or equal volume sterile water was added to cells for 16 hrs before 24 hrs post BAY timepoint. Leptomycin B (20 ng/ul, Sigma Aldrich; L2913) was added to RPE-1 or RPE-1 NES-GFP-NLS cells during 100 nM BAY treatment 5 hrs before fixing cells at 24 hrs post BAY timepoint. As a negative control an equal volume of sterile 100% ethanol was added to RPE-1 cells. For live imaging of RPE-1 NES-GFP-NLS cells imaging began when leptomycin B was added at 5 hrs before the 24 hrs post BAY timepoint. For GFP-NES imaging in U2OS cells, GFP-NES was transfected into U2OS cells using a 4D nucleofector (Lonza) and the SE cell line 4D-Nucleofector X Kit S (Lonza). Cells were trypsinized and pelleted. 200,000 cells were resuspended in buffer SE plus 400 ng plasmid, transferred to a 16-well electroporation cuvette, and electroporated using program DS-138. Cells were plated into penstrep free media and treated with 7.5 uM RO-3306 (Sigma-Aldrich; SML0569) for 16.5 hrs and released by washing 7x with warm media before live imaging and 20 ng/ul leptomycin B was added 2 hrs into imaging. RPE-1 or RPE-1 NES-GFP-NLS cells were synchronized with 1 uM PD for 24 hrs. 24 hrs later cells were transfected with RCC1-FLAG-H2A by nucleofection using a 4D nucleofector (Lonza) and the SE cell line 4D-Nucleofector X Kit S (Lonza). Cells were trypsinized and pelleted. 200,000 cells were resuspended in buffer SE plus 400 ng plasmid, transferred to a 16-well electroporation cuvette, and electroporated using program DS-138. Cells were plated into penstrep free media with 100 nM BAY and fixed for imaging 24 hrs later.

Plasmids

To construct pLVXE-Blast:2xRFP-NLS, mCherry-NLS-tagRFP sequence ordered as a G-Block from IDT and inserted in pLVXEblast (pLVXE-IRES-puro (Clontech) with puroR replaced by blastR) linearized by restriction digest at BamHI—EcoRI and assembled by Gibson assembly. pLVXE-Blast:TRE-RanT24N-mcherry was constructed by PCR and ligation of RanT24N-mcherry from pTK21 into a pLVXTight lentiviral vector (Clontech) previously modified to contain the Ef1a promoter and blasticidin gene. pTK12 was a gift from Iain Cheeseman (Addgene plasmid # 37396 ; http://n2t.net/addgene:37396 ; RRID:Addgene_37396). pLVX-Neo:Eto.1 was a gift from the Fred Gage lab (Salk Institute) and is pLVX-Tet-On Advanced (Clontech/Takara) with the CMV promoter replaced with the EF1a promoter. To construct pLVXE-neo:H2B-miRFP, H2B-miRFP703 was PCR'd out of pH2B-miRFP703 (a gift from Vladislav Verkhusha, (Addgene plasmid # 80001) and inserted into pLVXE-IRES-puro with the puroR replaced by neoR, using NotI/MluI restriction sites. pcDNA3.1:NLS-mCherry-LEXY (pDN122) was a gift from Barbara Di Ventura & Roland Eils (Addgene plasmid # 72655 ; http://n2t.net/addgene:72655 ; RRID:Addgene_72655). pLVXE-Blast: NES-GFP-NLS was constructed by PCR and ligation of CMV-NES-GFP-NLS from pcLumioDest:NES-GFP-NLS into a pLVXE lentiviral vector. pcLumioDest:NES-GFP-NLS was a gift from the Hetzer lab made by Gateway cloning. pDEST53:2xGFP-NES was characterized previously [42]. pLVE-Blast:TRE-RCC1-FLAG-H2A was created using vector builder (vector ID is VB240110-1335jye).

NLS-mcherry-LEXY live imaging and analysis

For NLS-mcherry-LEXY imaging 200,000 RPE-1 H2B-miRFP cells were nucleofected with 400 ng of NLS-mcherry-LEXY using the SE cell line 4D-Nucleofector X Kit S (Lonza) and DS-138 settings. After nucleofection cells were plated into a 2 well ibidi plate in penstrep free media. 8hrs later cells were treated with 100 nM BAY overnight for 16 hrs. At this point exposure to light was limited to prevent LEXY export and cells were kept in the dark for 15 minutes prior to imaging.

Images were acquired using a 40×/1.3 Plan Apo objective on an automated Leica DMi8 microscope outfitted with a Yokogawa CSU spinning disk unit, Andor Borealis illumination and an

ASI automated stage with Piezo Z-axis. Images were captured with an Andor iXon Ultra 888 EMCCD camera using MetaMorph software (version 7.10.4; Molecular Devices). RPE-1 H2B-miRFP cells expressing NLS-mcherry-LEXY were imaged every 30 seconds across 3 periods of time. To measure the starting LEXY intensity cells were imaged with Cy5 and sdRed channels for 5 min. Cells were then imaged with Cy5, dsRed, and DAPI lasers for 45 min to measure LEXY export. The DAPI channel was removed and cells were imaged for another 20 min with only Cy5 and dsRed to measure reimport of LEXY.

To quantify LEXY intensity in nuclei and MN throughout imaging the H2B-miRFP channel was used to create ROIs for nuclei and MN and the mcherry intensity in each ROI was quantified for all timepoints. To measure the cargo intensity for each cell, LEXY intensity in the cytoplasm was quantified at the end of the export period. The mean initial nuclear mean intensity and the nuclear area were calculated by averaging the first 5 intensity (LEXY) and area (H2B) values, respectively. The initial MN:N LEXY intensity ratio was calculated by dividing the MN and N mean intensities at the start of imaging. The plateau MN:N LEXY ratio (was calculated by dividing the MN and N mean intensities at the end of the export period.

To measure import rates, LEXY mean fluorescence intensity versus time was plotted for all nuclear compartments and fit to a one phase association curve in Prism (version 10.0.3). The curve fit the equation It = Imax * (1-e-kt) where I = fluorescence intensity, Imax = fluorescence intensity at the final plateau, and t = time. From this equation, the mean fluorescence value of Imax (plateau) and rate constant (k) were derived. The import rate was derived from the curve fit (initial rate = k*plateau). To measure export rates, LEXY mean fluorescence intensity versus time was plotted for all nuclear compartments and fit to a one phase decay curve from time 300 s to 2670 s in prism. The curve equation is It = I0 * e-kt where I = fluorescence intensity, I0 = fluorescence intensity at time 0, and t = time. From this equation, the mean fluorescence value of

I0 (the same as Y0 or Imax), the mean fluorescence value at the bottom of the curve (plateau) and rate constant (k) were derived. The initial export rate was calculated by a linear regression through the first 3 timepoints of export (300 s - 360 s) and recording the slope. Some curves did not initiate export immediately at 300 s. For curves with an overall negative slope between 300 s and 450 s the timepoints were shifted forward by 30 s until a negative slope was obtained.

Immunofluorescence

Cells were grown on poly-L-lysine coated coverslips and fixed in 4% PFA (Electron Microscopy Sciences) for 10 min at RT for the following experiments: RFP-NLS IF and IF+FISH in RPE-1 cells, NES-GFP-NLS IF in RPE-1 and U2OS cells and IF+FISH in RPE-1 cells, Ran IF and IF+FISH in RPE-1 cells, NPC IF in RPE-1 cells. IF and FISH experiments for RCC1 were pre-extracted for 15 seconds with 0.1% triton-X in 1xPBS then fixed for 10 min in 100% methanol at -20°C and refixed after secondary antibody staining with 4% pfa. For all other IF and FISH experiments, cells were fixed in 100% methanol at −20°C for 5–10 min. Coverslips were blocked in 3% BSA (Sigma-Aldrich) + 0.4% Triton X-100 (Sigma-Aldrich) + 0.02% sodium azide (Sigma-Aldrich) in 1× PBS (PBS-BT) for 30 min before incubation in primary antibodies diluted in PBS-BT.

Primary antibodies used: mouse or rabbit anti-H3K27ac (1:250; 1hr; 39085, Active Motif; 1:500; 30m; ab4729; Abcam), rabbit anti-H3K27me3 (1:500; 30m; MA511198; thermos fisher scientific), rabbit anti-H3K9me2 (1:250; 30m; AM39041; active motif), rabbit anti-Phospho-Rpb1 CTD (Ser2) (1:500; 30m; 13499S; Cell signaling technology), human anti-CREST (1:100; 1hr; 15-234; antibodies incorporated), rabbit anti-LBR (1:500; 30m; ab32535; abcam), rabbit anti-Lamin A (1:500, O/N at 4°C; L1293-200UL; sigma Aldrich), mouse anti-Ran (1:500; 4°C at O/N; MA511198; thermos fisher scientific), mouse anti-RCC1 (1:200; 2hrs, refix with 4% pfa; sc-376049; santa cruz biotechnology), rabbit anti-Nup133 (1:100; 30m; ab155990; abcam), rabbit anti-Nup153 (1:100; 30m; ab96462; abcam), rabbit anti-TPR (1:500; 30m; ab84516; abcam), rabbit anti-CRM1 (1:1000; 30m; 46249; Cell signaling technology), RFP-boost (1:1000; 1hr; rb2AF568; Chromotek), rabbit anti-FLAG (1:500; 30m; F7425; Millipore Sigma).

Coverslips were washed three times in PBS-BT then incubated in the following secondary antibodies: Alexa Fluor 647–conjugated goat anti-human (1:1000; 30m; A-21445; Thermo Fisher Scientific), Alexa Fluor 488–conjugated goat anti–mouse (1:1000; 30m; A-11029; Thermo Fisher Scientific), Alexa Fluor 405-conjugated goat anti-mouse (1:500; 1hr; A-31553; Thermo Fisher Scientific), Alexa Fluor 594–conjugated donkey anti-rabbit (1:500; 30m; 711-585-152; Jackson ImmunoResearch), Alexa Fluor 568-conjugated goat anti-mouse (1:1000; 30m; A11031; Life Technologies), Alexa Fluor 488–conjugated goat anti–rabbit (1:1000; 30m; A-11034; Thermo Fisher Scientific), Alexa Fluor 568-conjugated goat anti-rabbit (1:1000; 30m; A11036; Life Technol.ogies), Alexa Fluor 405-conjugated goat anti-rabbit (1:500; 1hr; A-31556; Thermo Fisher Scientific). Secondary antibodies were dilute in PBST and incubated for 30 min at RT. Coverslips were washed twice in PBST then incubated with DAPI (1 µg/ml in PBS; Roche) for 5 min at RT, washed once in diH_2O, and mounted in Vectashield (Vector Labs) or Prolong Gold (Life Technologies).

DNA-FISH

For experiments using chromosome enumeration (XCE) or whole chromosome paint (XCP) probes, after methanol fixation and immunofluorescence, as described above up until DAPI labeling, coverslips were fixed for 5 min with 4% PFA in 1× PBS. This and subsequent steps were performed at RT unless noted. Coverslips were washed twice with 2× SSC (Sigma-Aldrich) for 5 min then permeabilized with 0.2 M HCl + 0.7% Triton X-100 for 15 min at RT. Coverslips were washed twice with 2× SSC for 5 min, denatured in 50% formamide (EMD Millipore) 2× SSC for 1 hr, washed twice with 2× SSC, then inverted onto 3–5 µl of Spectrum Orange or green XCE or

XCP probe (MetaSystems) and sealed with rubber cement. Probes and targets were co-denatured at 74°C for 3 min and hybridized 2 hrs to overnight at 37°C in a humidified chamber (2 hrs for XCE probes and O/N for XCP probes). For methanol fixed cells coverslips were washed once in pre-heated 0.4× SSC buffer at 74°C for 5 min then twice in 2× SSC + 0.1% Tween-20 for 5 min. For pfa fixed cells coverslips were washed once in pre-heated 0.25× SSC buffer at 74°C for 5 min then twice in 4× SSC + 0.1% Tween-20 for 5 min. Coverslips were incubated in DAPI and mounted in Vectashield (Vector Labs) (for analysis of MN morphology or protein recruitment) or Prolong Gold (Life Technologies) (for MN rupture analysis).

Microscopy

Unless noted below, confocal images were acquired with a Leica DMi8 laser scanning confocal microscope using the Leica Application Suite (LAS X) software and a Leica ACS APO 40×/1.15 Oil CS objective or a Leica ACS APO 63×/1.3 Oil CS objective. Z-stacks were acquired with the system optimized step size except where noted.

MN rupture was analyzed from images taken on the Leica DMi8 with a z-step size of 0.5 um. Lamin A labeled cells for chr18 MN in hTERT-RPE-1 tetON Rant24n-mcherry cells – and + dox were imaged on the Leica DMi8 with a Leica ACS APO 63×/1.3 Oil CS objective and a z-step size of 0.2 um. Post-acquisition, images were deconvolved using lightning with smoothing a size of medium through the LAS X software.

Lamin A labeled cells for chr18 and 19 MN in DMSO, methylstat, and TSA treatments were imaged using a Leica TCS Sp8 with the super-resolution microscope system (STED) using a 775 nm pulsed laser, Leica Application Suite software platform (LAS X version 3.5.7.23225), and a Leica HC PL APO 100×/1.4 Oil CS2 objective. Before image acquisition the STED and confocal beams were manually aligned using FluoSpheres mounted in Prolong Gold and white light laser set to 594 and 775 nm STED, the alignment was adjusted until the STED FluoSpheres overlapped with the center of the confocal FluoSpheres images. Images were acquired at ~20 nm pixel size for a resolution of ~50 nm in the xy plane, and a white light laser was tuned to 405 nm (DAPI), 488 nm (H3K27ac), 556 nm (FISH), 594 nm (lamin A), and 647 nm (CREST) wavelengths. Post-acquisition, images were deconvolved using lightning with smoothing a size of medium through the LAS X software.

RCC1 labeled cells for chr19 MN in control and RCC1-H2A expressing cells were imaged using a Leica Stellaris, a Leica HC Plan Apo 63x / 1.40 Oil CS2 objective, and Leica Application Suite software platform (LAS X version 4.0.2).

For all images, post-acquisition image processing was limited to cropping the image and adjusting levels through Adobe Photoshop to make use of the entire histogram spectrum. False colors for channels were changed through the arrange channels function in Fiji [97].

Time lapse imaging

Unless noted below, time lapse images were acquired using a 40×/1.3 Plan Apo objective on an automated Leica DMi8 microscope outfitted with a Yokogawa CSU spinning disk unit, Andor Borealis illumination and an ASI automated stage with Piezo Z-axis. Images were captured with an Andor iXon Ultra 888 EMCCD camera using MetaMorph software (version 7.10.4; Molecular Devices). For hypotonic treatment RPE-1 RFP-NLS cells were imaged for single confocal slices at 2 min intervals for 2 hrs. For post mitotic MN and Nuclei growth U2OS GFP-NLS Lamin A-mcherry cells were imaged for the GFP channel imaged with z- stacks with a z-step size of 0.5 um at 3 min intervals. For leptomycin B treatment in U2OS NES-GFP cells were image with z-stacks with a z-step size of 2 um at 5 min intervals for 5 hrs. Leptomycin B treatment in RPE-1 NES-GFP-NLS cells was imaged for single confocal slices at 5 min intervals for 8 hrs.

Images for Lamin A gap growth in U2OS GFP-NLS Lamin A-mcherry cells were acquired using a 100x/1.4 (oil) objective on an Andor Dragonfly 200 High Speed Confocal Microscope. Images were capture with an Andor iXon 888 EMCCD using Fusion software and were taken every 10 minutes for z-stacks with a step size of 0.75 um.

Image quantification

An MN was defined as a DAPI positive round object adjacent to or near the nucleus that was distinct from the nucleus, to distinguish them from nuclear herniations and chromatin bridge fragments. Teardrop shaped objects were excluded from analysis. Intact MN were defined as those with H3K27ac mean intensity that was equivalent to that of the main nucleus over some part of its area or as those with LBR intensity equivalent to or lower than that of the main nucleus. Ruptured MN were defined as those where the average H3K27ac signal was decreased by >60% compared to the main nucleus or as those with LBR intensity higher than that of the main nucleus. Chromosome number was defined as the number of centromere foci, which were assessed by CREST IF. A positive FISH signal was defined as a focus twice the background signal that partially co-localized with a centromere. MN area was calculated from maximum intensity projections by selecting the DAPI channel object and measuring the area in FIJI. Pixel area was converted to μm^2 using the image dimensions.

Unless noted below protein intensity was quantified for intact (H3K27ac+) MN 24 hrs post-Cdk4/6i release into Mps1i and corresponding nuclei. Using FIJI, a single z-slice was analyzed from the middle of the MN. The DAPI or H3K27ac channel was used to create ROIs for nuclei or MN.

Fluorescence intensity in this region was measured and background subtracted measurements were obtained using a rolling ball radius of 50 pixels. The total intensity of histone modifications and RNA pol2 were quantified for intact (H3K27ac+) chr18 and 19 MN containing a single CREST focus that overlapped with the FISH probe 24 hrs post-Cdk4/6i release into MPS1i. Sum slices projections were analyzed and the DAPI channel as used to create ROIs for nuclei or MN and fluorescence intensity in this region was measured.

Bulk MN Ran intensity, chr18 and 19 MN Ran intensity, and chr 18 and 19 MN RCC1 intensity were quantified from z-stacks in Imaris ×64 8.4.2 (Bitplane). The intensities for intact (H3K27ac+), containing a single chromosome for FISH samples, 24 hrs post-Cdk4/6i release into Mps1i and its corresponding nucleus were quantified by first defining the region of interest for each MN and nucleus by creating a surface using the DAPI or H3K27ac channel. The smoothing was set to 0.5-0.8, and background subtraction of 0.4, and the threshold was adjusted to encompass the entire nuclear area. The mean intensity, total intensity, and volume for each surface were recorded.

The organization of H3K29me2 intensity in MN was measured for intact (H3K27ac+) containing a single chromosome 24 hrs post-Cdk4/6i release into Mps1i. Using FIJI, a single z-slice was analyzed from the middle of the MN. The H3K9me2 channel was used to create ROIs for MN and the MN area was divided into concentric shells 1 pixel wide. To measure the mean intensity the total florescence intensity of the H3K9me2 channel within each shell was measured and divided by the area of the shell. The number of shells was normalized to a 0-1 scale to compare different sized MN on the same scale.

Nuclear pore complex (NPC) protein density was determined for intact (H3K27ac+) MN 24 hrs post-Cdk4/6i release into Mps1i and its corresponding nucleus. The number of NPC foci per nucleus was quantified in Imaris ×64 8.4.2 (Bitplane) by first defining the region of interest around each MN and nucleus using the contour tool, then creating spots for each region of interest with a XY spot diameter set to 0.22 μM. The threshold was adjusted for each image to capture every NPC focus in the nucleus but very few spots in the cytoplasm. The same threshold was used for the corresponding MN. The surface area was calculated in Imaris from the DAPI channel, with smoothing set to 0.8, and background subtraction of 0.4, and the threshold adjusted to encompass the entire DAPI signal.

Nuclear lamina gaps in chr18 and 19 MN and after histone drug treatments were quantified using a previously established MATLAB pipeline [42]. Nuclear gaps in chr18 MN after RanT24N expression were quantified using a MATLAB app previously used for lamina gap identification in the nucleus [98].

Methods used to calculate mutational signatures of chromothripsis

Single nucleotide variant (SNV) data from 50 cancer cohorts from Pan-Cancer Analysis of Whole Genomes (PCAWG) Consortium was downloaded [99]. Furthermore, annotations for chromothripsis events were also matched to coded patient ID i.e. ICGC donor ID [91] leading to a total of 2987 chromothripsis events across 1019 patients across 50 cancer cohorts. Chromothripsis events were annotated for:

- ‘High confidence’
- ‘Low confidence’
- ’Linked to high confidence’ and
- ‘Linked to low confidence’

Only ‘high confidence’ annotated chromothripsis events were selected for analysis and compared to those with annotations of ‘no’ chromothripsis events.

Additional chromothripsis annotations are:

- ‘Before polyploidization’
- ‘After polyploidization’
- ‘Canonical without polyploidization’ and
- ‘With other complex events’

‘With other complex events’ was removed from the dataset to remove any confounding factors due to other complex events.

Chromosomes were categorized into the following categories based on the hypothesized timing of rupture of micro-nuclei containing the respective chromosomes:

- Early rupture: '13', '18', '21'
- Late rupture: '1','2','3','4','5','6','17','19','X'
- Mid rupture: '7','8','9','10','11','12','14','15','16','20','22'

The filtered dataset results in the following distribution of high confidence chromothripsis events without any other complex events:

Early Rupture	**Mid rupture**	**Late Rupture**
74	256	332

Sigprofiler [100] was used to assign COSMIC signatures version 3.4 to the SNVs. SNVs in each patient were assigned one of six categories, which were a combination of chromothripsis status of ‘yes’ or ‘no’ and chromosome status of ‘early’, ‘mid’ or ‘late’ rupture. SNVs in each category of the sample were assigned to mutational signatures, which were then normalized by the total number of SNVs in the sample category. The normalized proportion of SNVs assigned to APOBEC signature (SBS 2 and SBS 13) were averaged across early, mid and late rupture chromosomes that are chromothripsis positive. Code to process the data can be found on a public repository here: https://github.com/manasvitavashisth/MutationalSignatureAnalysis

Statistics

All statistic tests were conducted using R (version 4.0.0) or Prism (version 10.0.3). For all tests, P-values greater than 0.05 were considered statistically significant. For all data comprising three or more groups of observations, a family test (i.e., chi-squared for categorical data, ANOVA test for continuous data) was performed first to test the null hypothesis that all the observations were the same. Only data where the family test rejected the null hypothesis were further analyzed by multiple comparison testing. For statistical analysis of categorical data between 2 groups, p-values were calculated using Barnard's exact test on R (version 3.4.1). For statistical analysis of the distribution of quantitative data between 2 groups where one or more groups deviated from normality, p-values were calculated with Wilcoxon rank sum test on R (version).

For statistical analysis of the distribution of paired quantitative data (e.g., paired MN-Nuc data from LEXY imaging) p-values were calculated with the paired Wilcoxon rank sum test on R. To compare MN:Nuc ratios to the null hypothesis of 1, p-values were calculated with a one sample Wilcoxon ran sum test on R. Spearman's rank correlation coefficient was used to assess monotonic relationships for two variables with non-normal distribution (e.g., LEXY intensity vs transport rates, fluorescence intensity vs MN areas) with R or prism. To compare the slopes of regression lines (e.g., LEXY transport data vs cargo concentration) a simple linear regression and the Analysis of Covariance (ANCOVA) test were performed in prism.

For analysis of chromothripsis mutational signatures the Anova test using the R function 'aov' was used to identify difference in the categoric data sets. Moreover, Turkey Honest Significant Differences test was used to used ascertain statistically significant differences in the increase in

APOBEC signature proportion in the early rupture chromosomes undergoing chromothripsis compared to mid and late rupture. Additionally, chromothripsis negative chromosomes do not show any statistically significant differences in APOBEC signature in early, mid and late rupture chromosomes.

Chapter 3 : The contribution of chromosome identity to micronucleus formation

Abstract

Micronuclei form when missegregated chromatin recruits its own nuclear envelope at the end of mitosis. Micronuclei are potent drivers of chromothripsis, the fragmentation and random reassembly of chromosomes, which occurs at high frequencies in a variety of cancers and is an initiating event in several brain cancers. We have previously found that micronucleation of different chromosomes affects rupture frequency, signifying that the identity of the micronucleated chromosome along with the frequency of micronucleation significantly impacts the acquisition of genome alterations in cancer. Together these data strongly support the critical need to understand how micronuclei form in cancer tissue and which chromosomes they contain. Previous work from our lab and others has shown that chromosome missegregation and micronucleation after mitotic disruption are non-random, however the mechanism of micronucleation bias has not been investigated. We find that MN formation after spindle assembly checkpoint (SAC) inhibition is biased for chromosomes 1, 4, 13, and 18, while MN formation after merotelic attachment is mainly biased for chromosome 1. These results support micronucleation as a non-random process. Further work identifying the mechanism behind unique MN biases will enable new insight into the role of micronuclei in driving tumorigenesis through genome alteration.

Introduction

Micronuclei form when missegregated chromosomes recruit their own nuclear envelope. Micronuclei have many features of normal nuclei, but are defective in DNA replication and kinetochore assembly, driving aneuploidy of the isolated chromosome(s) [50,52,53]. The membranes of micronuclei are unstable and frequently rupture [16], which has been linked to an innate immune response, and specifically the inflammatory abscopal response, along with increased expression of epithelial-mesenchymal transition genes [32,101]. In addition, micronucleus rupture causes chromosome fragmentation and is likely a major mechanism of chromothripsis [29], which involves fragmentation and random reassembly of chromosomes and is observed in a wide variety of cancers [102]. Therefore, micronuclei directly connect mitotic errors and cancer development as their rupture leads to genome instability and inflammation, the two enabling characteristics for tumorigenesis [21]. Our lab has identified that chromosome content influences micronucleus stability [42]. However, our knowledge of which chromosomes are enriched in micronuclei and the mechanism by which specific chromosomes are preferentially missegregated into micronuclei is not complete. In part, this is because the general mechanisms of micronucleation versus missegregation have not been elucidated. Micronuclei are a diagnostic criteria and chromothripsis rearrangements have been documented to cause cancer driving mutations [103–105], which strongly supports the critical need to understand how frequently micronuclei form and contribute to cancer genome evolution.

Missegregated chromosomes fail to properly segregate during anaphase. The most common form is lagging chromosomes, which arise through improper microtubule attachments or improper chromatid separation, though unaligned and unattached chromatin also contribute to missegregation. Missegregation can lead to aneuploidy, in which the chromosome is segregated into the incorrect daughter cell, and/or micronucleation, where the chromosome remains isolated from the primary chromosome mass. Recurrent gains, losses, and translocations of specific chromosomes are a defining feature of many cancer types. However, it is not known how much of missegregation and aneuploidy in cancer is due to initial micronucleation of chromosomes as opposed to selection. Also, few mechanisms promoting or preventing micronuclei have been identified despite micronucleation having more severe outcomes compared to missegregation and aneuploidy alone.

Specific chromosome features cause non-random chromosome missegregation. For example, extension of prometaphase leads to missegregation and aneuploidy of the 2 largest human chromosomes, chromosomes 1 and 2, due to cohesion fatigue [66] while chromosomes with large centromeres missegregate more frequently after mitotic disruption due to the formation of more erroneous microtubule kinetochore attachments [67]. Chromosome features have not yet been studied for their contribution to micronuclei formation, but evidence for a bias in micronucleation is supported by the enrichment of specific chromosomes in micronuclei isolated from healthy human tissue [106–108]. A current limitation of these studies is that they are limited to one form of mitotic disruption, only identify micronuclei that permit cell proliferation, and don't accurately reflect initial chromosome micronucleation levels. Thus, the true rate of chromosome micronucleation it is not known. Also, the mechanism behind biased incorporation of chromosomes into micronuclei has not been identified. Specific chromosome features influence biased missegregation [66–69], but whether micronucleation bias is due to similar chromosome features or is a product of the mitotic machinery has not been determined. Here we begin to develop more comprehensive approaches to look at all chromosomes in MN across multiple mitotic disruptions. Completing these studies will be essential to identifying whether missegregation and micronucleation follow the same biases and the factors that influence micronucleation bias specifically.

Results

MN content is non-random

We focused on identifying MN formation after 2 main mechanisms: Merotelic microtube attachment and SAC deficiency. These two mechanisms of micronuclei formation have also been identified as drivers of chromosomal instability in cancer [109]. Merotelic attachments occur when one sister chromatid is bound by microtubules from both spindle poles and are the primary cause of chromosome instability in cancer tissue [110]. These attachments are caused by mislocalization of kinetochore-microtubule attachment proteins or errors in spindle geometry during formation of the bipolar mitotic spindle. To identify the chromosomes micronucleated due to merotelic microtubule attachment in human cells we treated cells with nocodazole, a drug inhibiting microtubule polymerization that causes mitotic delay resulting in both sister chromatid cohesion fatigue and increased levels of merotelic attachments after washout. The SAC ensures proper chromosome segregation by preventing anaphase onset in the presence of unattached kinetochores [111]. Misexpression of SAC genes has been identified in cancer cells isolated from multiple tissues and their disruption has been linked to increased levels of chromosome missegregation [112–114]. To test the effect of SAC deficiency on chromosome specific micronucleation we treated cells with reversine a small molecule inhibitor of monopolar spindle kinase 1 (Mps1), an upstream regulator of the SAC. RPE-1 cells were used for these experiments because they are diploid, rarely form micronuclei spontaneously, and are karyotypically stable.

To determine whether micronuclei are enriched in specific chromosomes, we used chromosome specific DNA-FISH probes to target a subset of human chromosomes in RPE-1 cells after nocodazole and reversine treatments (Fig. 3.1a). For each treatment, individual chromosomes are found to be enriched or depleted compared to what is expected for random micronucleation (4.3%), supporting that micronucleation is a non-random process. Reversine caused enrichment of chromosome 1, 4, 13, 18, and 20 while nocodazole MN were mainly enriched for chromosomes 1 and 11 (Fig. 3.1b). These results suggest that different mitotic disruptions have different effects on micronucleus content and, importantly, they do not align with patterns of missegregation found in previous studies [66], suggesting separate biases for each process.

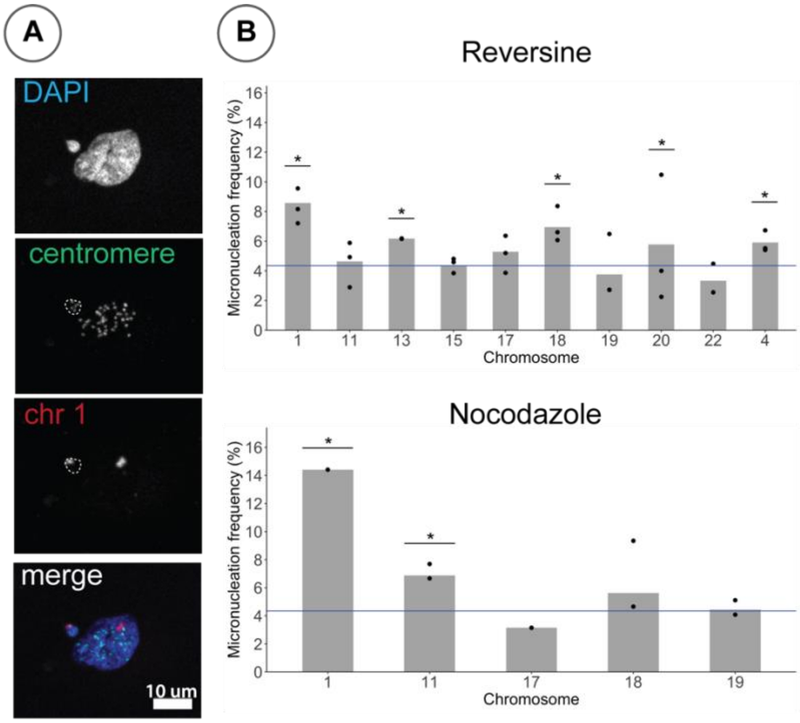

Figure 3.1: Non-random micronucleation of human chromosomes.

A. Representative DNA FISH image of micronucleated chromosome 1. **B.** Micronucleation frequencies from DNA FISH. Blue bar represents random (4.3%) micronucleation. Chi-square for goodness of fit test. Reversine: n=(1015, 592, 991, 616, 686, 813, 849, 663, 588, 330). Nocodazole: n=(111, 451, 127, 515, 382). For all graphs, ns $p>0.05$, * $p<0.05$, ** $p<0.01$, *** $p<0.001$, **** $p<0.0001$.

Subcellular fractionation and TigerFISH

To follow up on our preliminary results identifying a bias in MN formation, we next wanted to look at all 23 chromosomes after multiple mitotic disruptions. A challenge with our previous assay is targeting chromosomes individually with DNA FISH probes. To address this issue we planned to apply 2 techniques that overcome these limitations: subcellular fractionation with DNA sequencing and TigerFISH.

I first applied a subcellular fractionation technique to address this question. This protocol lysed open RPE-1 cells treated with DMSO, nocodazole, or reversine and separated MN from nuclei by size through a series of sucrose gradients. The DNA from isolated MN could then be sequenced to identify chromosome content. Subcellular fractionation of micronuclei has been used for proteomic analysis by other labs [26,76]. However, after optimization of this protocol we concluded that subcelluar fractionation was not the best tool to screen MN content after multiple types of mitotic disruption as the amount DNA recovered at the end of this was insufficient for DNA sequencing. The only way to overcome this would be to increase the number of cells at the start of the experiment, however the number of cells needed for each treatment is too high for this to be a feasible experiment to assay multiple treatments at once.

We next planned to identify the micronucleation frequency of all 23 human chromosomes after each drug treatment using TigerFISH, a DNA FISH technique developed by the Beliveau lab [115]. For this technique the Beliveau lab designed an algorithm to identify FISH probe sequences targeting repeats located in satellite DNA for each chromosome and are tested the specificity of these probes on metaphase spreads (Fig. 3.2a,b). These probes can be combined with SABER technology [116] and microfluidic probe exchange to allow for rapid analysis of micronucleus content and enable high throughput analysis of micronucleation across multiple conditions.

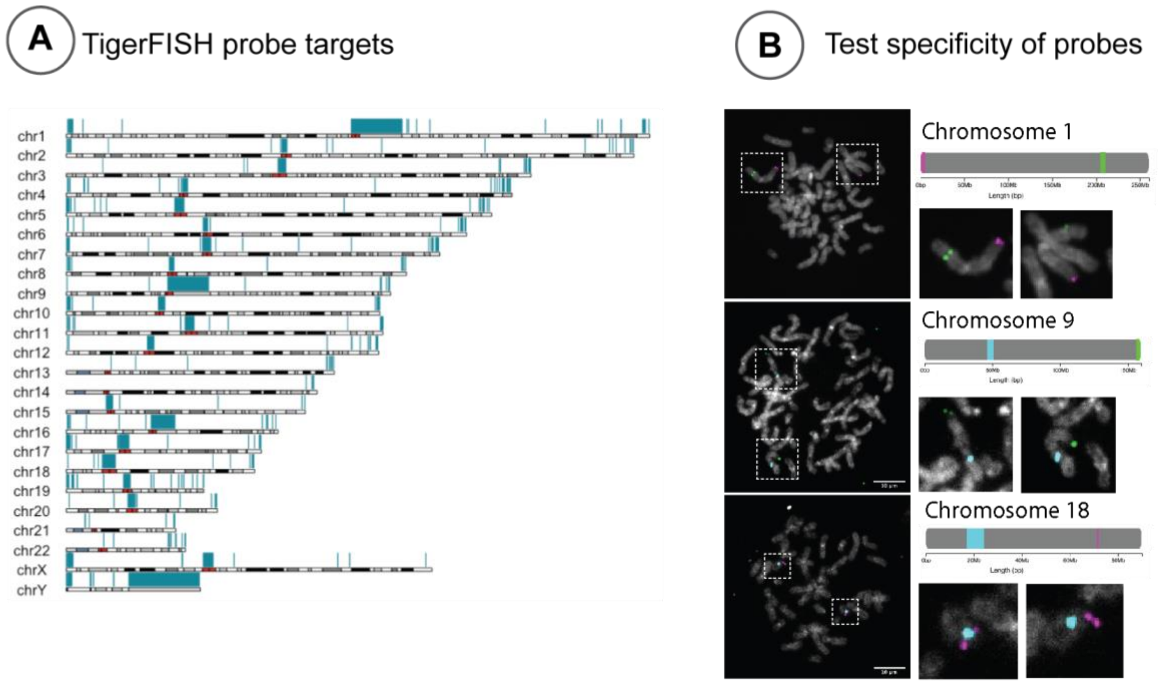

Figure 3.2: TigerFISH validation

A. Regions where oligo probes were designed against satellite DNA (blue). Red squares are indicative of centromeric sequence; black and gray bars are cytogenetic bands. **B.** Test for specificity of 2 potential probes for chr1, 9, and 18 on human metaphase spreads using TigerFISH and SABER. Insets show labeled chromosomes and diagram outlines location of probes on each chromosome. Chromosomes are identified by cytogenetics.

In collaboration with the Beliveau lab, I began testing the specificity of TigerFISH probes targeted against satellite regions of DNA in interphase RPE-1 cells. Preliminary experiment showed specificity of probes targeting chromosome 1 and 18. Further work testing additional probes and comparing chromosome number and relative position to known chromosome territories [117] will validate this method in interphase cells. Using TigerFISH to identify MN content would be advantageous because it also identifies co-micronucleation frequencies for chromosomes and could be applied to other systems, such as tissue or organoid samples.

Discussion

After this project was set aside, another group performed a similar analysis looking at chromosome bias in missegregation and MN formation using a combination of single-cell DNA sequencing, isolation of MN, and DNA-FISH probes [68]. This study focused on missegregation after Mps1 inhibition in RPE-1 cells and found large chromosomes, such as 1-5, 8, 11, and X, to be biased toward both missegregation and MN formation. These results slightly differ from our FISH analysis, where see also see enrichment of smaller chromosomes such as chr18. Interestingly, they find that this bias is due to interphase nuclear location, where chromosomes near the nuclear periphery are more likely to both missegregate and form MN. Chromosome 18 is also near the nuclear periphery in interphase, in line with this model. It is possible that this mechanism is also responsible for MN bias seen in our preliminary studies, though completing this analysis for all chromosomes would be needed to confirm this. Whether this bias is also responsible for the enrichment of large chromosomes in MN after nocodazole treatment, or if other mechanisms connected to large chromosome missegregation such as cohesion fatigue may be more dominant in this process, is not known. Investigating whether this mechanism causing chromosome specific micronucleation is altered in different contexts, such as after different mitotic errors or in different cell types, will define the requirements for MN formation in cells. This will add to our understanding of how micronuclei contribute to cancer development and progression while also allowing for the prediction of chromosomes likely to be impacted by mitotic errors in cancer tissue.

Subcellular fractionation of MN for protein analysis was recently applied to identify nuclear processes disrupted in MN [71] proving its strength as a tool for discovery in the MN field. This tool could be applied to address additional questions proposed in this work, such as better defining how the MN export defect is established or for identifying what the eventual rupture trigger is in MN.

Methods

Cell lines and culture methods

hTERT-RPE-1 (RRID: CVCL_4388) cells were grown in DMEM/F12 (Gibco) + 10% FBS (Gibco) + 1% Pen-Strep (Gibco) + 0.01 mg/ml hygromycin (Sigma-Aldrich) at 5% CO_2 and at 37°C. To induce MN for RPE-1 IF and IF+FISH experiments and U2OS IF experiments cells were arrested in G1 by addition of 1 μM PD-0332991 isethionate (Cdk4/6i; Sigma-Aldrich) for 24 hrs. Cells were released by washing three times in 1× PBS before incubation in 0.5 μM reversine (Mps1i; EMD Millipore) for 20 hrs. For nocodazole treatment and missegregation position experiments, RPE-1 cells were incubated in 1 ug/ml nocodazole (Sigma-Aldrich) for 14hrs prior to release by washing three times with 1× PBS and then adding either media alone (nocodazole) or media for 6hrs.

Immunofluorescence

Cells were grown on poly-L-lysine coated coverslips and fixed in 4% PFA (Electron Microscopy Sciences) for 10 min at RT. Coverslips were blocked in 3% BSA (Sigma-Aldrich) + 0.4% Triton X-100 (Sigma-Aldrich) + 0.02% sodium azide (Sigma-Aldrich) in 1× PBS (PBS-BT) for 30 min before incubation in primary antibodies diluted in PBS-BT. Primary antibodies used: mouse or rabbit anti-H3K27ac (1:250; 1hr; 39085, Active Motif; 1:500; 30m; ab4729; Abcam) and human anti-CREST (1:100; 1hr; 15-234; antibodies incorporated). Coverslips were washed three times in PBS-BT then incubated in the following secondary antibodies: Alexa Fluor 647–conjugated goat anti-human (1:1000; 30m; A-21445; Thermo Fisher Scientific), Alexa Fluor 488–conjugated goat anti–mouse (1:1000; 30m; A-11029; Thermo Fisher Scientific), Alexa Fluor 488–conjugated goat anti–rabbit (1:1000; 30m; A-11034; Thermo Fisher Scientific). Secondary antibodies were dilute in PBST and incubated for 30 min at RT. Coverslips were washed twice in PBST then incubated with DAPI (1 μg/ml in PBS; Roche) for 5 min at RT, washed once in diH_2O, and mounted in Prolong Gold (Life Technologies).

DNA-FISH

For experiments using chromosome enumeration (XCE) or whole chromosome paint (XCP) probes, after methanol fixation and immunofluorescence, as described above up until DAPI labeling, coverslips were fixed for 5 min with 4% PFA in 1× PBS. This and subsequent steps were performed at RT unless noted. Coverslips were washed twice with 2× SSC (Sigma-Aldrich) for 5 min then permeabilized with 0.2 M HCl + 0.7% Triton X-100 for 115 min at RT. Coverslips were washed twice with 2× SSC for 5 min, denatured in 50% formamide (EMD Millipore) 2× SSC for 1 h, washed twice with 2× SSC, then inverted onto 3–5 μl of Spectrum Orange or green XCE or XCP probe (MetaSystems) and sealed with rubber cement. Probes and targets were co-denatured at 74°C for 3 min and hybridized 2 h to overnight at 37°C in a humidified chamber (2hrs for XCE probes and O/N for XCP probes). Coverslips were washed once in pre-heated 0.4× SSC buffer at 74°C for 5 min then twice in 2× SSC + 0.1% Tween-20 for 5 min. Coverslips were incubated in DAPI and mounted in Vectashield (Vector Labs) (for analysis of MN morphology or protein recruitment) or Prolong Gold (Life Technologies) (for MN rupture analysis).

Outline of subcellular fractionation of MN

For MN isolation, four 15cm plates of hTERT-RPE-1 cells were plated for each condition. To induce MN cells were arrested in G1 by addition of 1 μM PD-0332991 isethionate (Cdk4/6i; Sigma-Aldrich) for 24 hrs. Cells were released by washing three times in 1× PBS before incubation in 0.5 μM reversine (Mps1i; EMD Millipore), 1 ug/mL nocodazole (Sigma-Aldrich), or DMSO for no treatment control for 20 hrs. Nocodazole treated cells were washed three times in 1× PBS 6 hours before starting the protocol and released into normal media. Prior to collecting cells all conditions were treated with 10 μM RO-3306 (Sigma-Aldrich; SML0569) for 2 hrs to deplete mitotic cells and with 1 μg/mL cytochalasin D and 1ug/mL nocodazole for 1hr prior to collection to depolymerize the cytoskeleton. Cells were trypsinized and pelleted for 5 m at 1.2 krpm 4˚C, washed in ice cold 1× PBS and pelleted again. The pellet was suspended in 1 mL NP40-lysis buffer on ice for 15 min in a BSA coated tube. Cells were lysed by passing cell suspension through two 1 mL syringes attached to 23 1½ g needles connected by a short piece of plastic tubing 5 times. To pellet the nuclei out of the whole cell lysate 111 μL 2.3M sucrose/1 mL of cell lysate was added and the lysate was centrifuged for 10 m 2 kg 4˚C. The supernatant and the flocculent pellet of whole cells was removed from the top of the nuclear pellet. The nuclear pellet was resuspend in 500 μL 1M sucrose, placed over a 1 mL 1.8M sucrose cushion, and spun at 30 m 43 krpm at 4˚C in a TLS-55 rotor. After spin, the top layer of the gradient was removed, the top of the cushion was washed with ~300ul of TKM buffer (50 mM Tris pH 7.5, 25 mM KCl, 5 mM $MgCl_2$) 3 times and the rest of the supernatant was removed. The pellet was resuspended in 200 μL 0.5 M sucrose and placed over a 2 mL discontinuous sucrose gradient: 1 mL 2.3 M sucrose then 1 mL 1.4 M sucrose. Gradient was spun 30 m 4˚C 5krpm. We collected 100 μL fractions from the top of the gradient and put each in its own tube and then resuspend the pellet in 100μL of 0.5 M sucrose. Fractions wer stored at -80˚C. MN are located be in upper fractions, PN will be at bottom/pelleted and the contents of each fraction was assayed with microscopy by taking 2uL of the fraction + 1uL DAPI. Fractions containing only MN or PN were combined, diluted10x in TKM buffer, and spun at 10 m 20 kg 4˚C to pellet nuclei for immunofluorescence or DNA isolation.

Statistics

All statistic tests were conducted using R (version 4.0.0). For all tests, P-values greater than 0.05 were considered statistically significant. For all data comprising three or more groups of observations, a family test (i.e., chi-squared for categorical data) was performed first to test the null hypothesis that all the observations were the same. Only data where the family test rejected the null hypothesis were further analyzed by multiple comparison testing. For statistical analysis of categorical data, MNation frequency for each chromosome was compared to random (4.3%) and p-values were calculated using Barnard's exact test on R (version 3.4.1).

Chapter 4 : Conclusions and future directions

The influence of gene density on MN stability

We find that histone modifications are a key determinate of gene density differences in MN stability. Specifically, increasing histone methylation in MN leads to instability and defects in lamina organization. An essential next step to understanding MN stability will be to address why the stiffness associated with heterochromatin is detrimental to MN stability, rather than beneficial [73]. Future studies should identify whether this difference in chromatin's effect on stability is mainly due to growth differences, as outlined in this work, or if additional mechanisms contribute to these changes. Possible alternative mechanisms could include altered mechanical forces in MN due to overcompaction [40,41,93] or a disruption to the expected chromatin-lamina interactions in MN.

The origin of lamina gaps in MN

We identify growth as a new mechanism promoting lamina defects in MN. This method of lamina gap formation is unique to MN, as nuclei are able to control their size and don't experience overgrowth like MN. We don't know whether growth is sufficient for MN rupture, however additional experiments manipulating growth and determining the effect on both lamina gap appearance and growth will strengthen our understanding of this pathway. Lamina gaps are present in intact MN prior to rupture, suggesting they may not be sufficient for rupture. Testing this hypothesis will be an essential next step in this project. If lamina gaps are not sufficient for MN rupture, novel rupture triggers could be identified through subcellular fractionation and proteomics to identify unique MN proteins or by testing proteins already known promote MN rupture, such as ATR [18] or Chmp7, to test if they are working in this same pathway.

Defective nuclear export in MN

We find that only export is largely altered in MN in RPE-1 and U2OS cells, in contrast to other studies that find an import defect in MN [17,52]. Our reporters for import are small in size and some proteins found to be lost from MN are very large. Large proteins are more sensitive to changes in the Ran gradient [58], and therefore it is possible that we are missing a large protein import defect in our studies. Similar to previous studies [16,17,42,48,50,54] we do see a depletion of nuclear pores in MN. Additionally, the extent of import ability in MN may differ based on the method of MN formation, which has been shown to influence growth potential in MN [62]. Confirming our export defect is present after MN formation from nocodazole treatment in RPE-1 cells would be a good first step to test this possibility.

We observe a continuous growth defect for MN, which is likely unique to MN because of their location in the same cytoplasm as a fully functioning nucleus. Studies that inhibit nuclear export [85] or induce RCC1 loss [89] find a limit to nuclear growth or accumulation of proteins and don’t report nuclear rupture. The cellular environment of MN therefore may enhance transport defects and their consequences. This association between nuclei and MN could also lead to competition for protein access, which could possibly contribute to defects in nuclear functions, including loss of RCC1 from MN. Taking advantage of experimental systems that increase transport cargo access, such as the permeabilized cell assay where the plasma membrane of cells is permeabilized and exogenous cytoplasm is added to cells [118,119], can give us sight into this relationship by relieving competition between these nuclear compartments.

Further work looking at origin of the export defect in MN is needed to determine if RCC1 loss is the main cause. This has been difficult for us to identify because RCC1 is an essential protein necessary for both mitotic spindle formation and NE reformation [120,121], so it cannot be largely manipulated in cells without additional consequences that inhibit studying MN function. RCC1 is located in the nucleus through 2 mechanisms. RCC1 is bound to chromosomes during mitosis and also is also imported into nuclei after the nuclear envelope is resealed [122]. Our preliminary data show that RCC1 levels in MN decrease over time. This suggests an issue with RCC1 maintenance, rather than recruitment. Most MN can import at similar levels to nuclei, suggesting that lack of import is not the main reason for RCC1 depletion in MN. However, RCC1 import could be low due to competition with the nucleus. Testing this hypothesis will strengthen our model by defining RCC1's role in MN rupture.

MN rupture in cancer

Based on the data presented in this work, we propose that MN rupture timing is an important contributor to the lasting consequences of MN rupture in vivo. Work looking at biases in MN content, from this project and others [68], finds that chromosomes near the nuclear periphery, which are normally heterochromatic, are enriched in MN. We find that heterochromatic chromosomes rupture early and acquire more APOBEC mutations during chromothripsis. Together this suggest that early rupturing chromosomes are commonly found in MN and likely make a significant contribution to MN rupture consequences in cancer tissues. In addition, we find that euchromatic chromosomes are stable and delay rupture due to a defect in growth. This stability is also seen in double minute chromosome MN, which are small, euchromatic, and rarely rupture [95]. The mechanism behind small gene rich MN stability we have uncovered here might be applicable in these unique MN. To test whether the mechanisms of MN rupture outlined in this project are at work in double minute MN, future work should characterize growth and lamina organization in these MN. Additionally, testing whether their stability is decreased by methylstat treatment, similar to chr19 MN, would determine whether the histone modification rupture pathway identified in this work is function in these MN.

Conclusions

This project describes the contribution of chromosome identify to MN formation, function, and rupture. The findings presented here identify a novel pathway for MN rupture, MN transport, and connect transport levels to chromosome identity through histone modifications. This work begins to define how transport contributes to lamina organization defects and instability. Additional mechanisms that promote MN rupture will likely interact with the mechanism described here and connecting these processes will be key in pushing the MN field further. Elucidating the causes of MN rupture will allow to us transfer this knowledge to in vivo systems, connecting MN formation and rupture to the consequences in cancer tissue.

References

1. Zhao G, Liu S, Arun S, Renda F, Khodjakov A, Pellman D: **A tubule-sheet continuum model for the mechanism of nuclear envelope assembly**. *Dev Cell* 2023, **58**:847-865.e10.

2. Sommer S, Buraczewska I, Kruszewski M: **Micronucleus Assay: The State of Art, and Future Directions**. *Int J Mol Sci* 2020, **21**:1534.

3. Merta H, Rodríguez JWC, Anjur-Dietrich MI, Vitale T, Granade ME, Harris TE, Needleman DJ, Bahmanyar S: **Cell cycle regulation of ER membrane biogenesis protects against chromosome missegregation**. *Dev Cell* 2021, **56**:3364-3379.e10.

4. Maheshwari R, Rahman MM, Drey S, Onyundo M, Fabig G, Martinez MAQ, Matus DQ, Müller-Reichert T, Cohen-Fix O: **A membrane reticulum, the centriculum, affects centrosome size and function in Caenorhabditis elegans**. *Curr Biol* 2023, **33**:791-806.e7.

5. Ferrandiz N, Downie L, Starling GP, Royle SJ: **Endomembranes promote chromosome missegregation by ensheathing misaligned chromosomes**. *J Cell Biol* 2022, **221**:e202203021.

6. Gomes AM, Orr B, Novais-Cruz M, Sousa FD, Macário-Monteiro J, Lemos C, Ferrás C, Maiato H: **Micronuclei from misaligned chromosomes that satisfy the spindle assembly checkpoint in cancer cells**. *Curr Biol* 2022, **32**:4240-4254.e5.

7. Knouse KA, Lopez KE, Bachofner M, Amon A: **Chromosome Segregation Fidelity in Epithelia Requires Tissue Architecture**. *Cell* 2018, **175**:200-211.e13.

8. Warecki B, Sullivan W: **Mechanisms driving acentric chromosome transmission**. *Chromosom Res* 2020, **28**:229–246.

9. Maiato H, Afonso O, Matos I: **A chromosome separation checkpoint**. *Bioessays* 2014, **37**:257–266.

10. Guo X, Ni J, Liang Z, Xue J, Fenech MF, Wang X: **The Molecular Origins and Pathophysiological Consequences of Micronuclei: New Insights into an Age-old Problem**. *Mutat Res Rev Mutat Res* 2018, **779**:1–35.

11. Yano S, Akiyama K, Tsuchiya R, Kubotani H, Chiba T, Nagata T, Tsuruta F: **A MATLAB-based program for three-dimensional quantitative analysis of micronuclei reveals that neuroinflammation induces micronuclei formation in the brain**. *Sci Rep* 2021, **11**:18360.

12. Bolognesi C, Lando C, Forni A, Landini E, Scarpato R, Migliore L, Bonassi S: **Chromosomal damage and ageing: effect on micronuclei frequency in peripheral blood lymphocytes.** *Age ageing* 1999, **28**:393–397.

13. Fenech M, Morley AA: **The effect of donor age on spontaneous and induced micronuclei**. *Mutat ResFundam Mol Mech Mutagen* 1985, **148**:99–105.

14. Liu B, Wang J, Chan KM, Tjia WM, Deng W, Guan X, Huang J, Li KM, Chau PY, Chen DJ, et al.: **Genomic instability in laminopathy-based premature aging**. *Nat Med* 2005, **11**:780–785.

15. Meaburn KJ, Cabuy E, Bonne G, Levy N, Morris GE, Novelli G, Kill IR, Bridger JM: **Primary laminopathy fibroblasts display altered genome organization and apoptosis**. *Aging Cell* 2007, **6**:139–153.

16. Hatch EM, Fischer AH, Deerinck TJ, Hetzer MW: **Catastrophic Nuclear Envelope Collapse in Cancer Cell Micronuclei**. *Cell* 2013, **154**:47–60.

17. Liu S, Kwon M, Mannino M, Yang N, Renda F, Khodjakov A, Pellman D: **Nuclear envelope assembly defects link mitotic errors to chromothripsis**. *Nature* 2018, **561**:551–555.

18. Joo YK, Black EM, Trier I, Haakma W, Zou L, Kabeche L: **ATR promotes clearance of damaged DNA and damaged cells by rupturing micronuclei**. *Mol Cell* 2023, doi:10.1016/j.molcel.2023.09.003.

19. Vietri M, Schultz SW, Bellanger A, Jones CM, Petersen LI, Raiborg C, Skarpen E, Pedurupillay CRJ, Kjos I, Kip E, et al.: **Unrestrained ESCRT-III drives micronuclear catastrophe and chromosome fragmentation**. *Nat Cell Biol* 2020, **22**:856–867.

20. Willan J, Cleasby AJ, Flores-Rodriguez N, Stefani F, Rinaldo C, Pisciottani A, Grant E, Woodman P, Bryant HE, Ciani B: **ESCRT-III is necessary for the integrity of the nuclear envelope in micronuclei but is aberrant at ruptured micronuclear envelopes generating damage**. *Oncogenesis* 2019, **8**:29.

21. Hanahan D, Weinberg RA: **Hallmarks of Cancer: The Next Generation**. *Cell* 2011, **144**:646–674.

22. Vashi N, Bakhoum SF: **The Evolution of STING Signaling and Its Involvement in Cancer**. *Trends Biochem Sci* 2021, **46**:446–460.

23. Tang S, Stokasimov E, Cui Y, Pellman D: **Breakage of cytoplasmic chromosomes by pathological DNA base excision repair**. *Nature* 2022, **606**:930–936.

24. Umbreit NT, Zhang C-Z, Lynch LD, Blaine LJ, Cheng AM, Tourdot R, Sun L, Almubarak HF, Judge K, Mitchell TJ, et al.: **Mechanisms generating cancer genome complexity from a single cell division error**. *Science* 2020, **368**:eaba0712.

25. Deng L, Wu RA, Sonneville R, Kochenova OV, Labib K, Pellman D, Walter JC: **Mitotic CDK Promotes Replisome Disassembly, Fork Breakage, and Complex DNA Rearrangements**. *Mol Cell* 2019, **73**:915-929.e6.

26. Mohr L, Toufektchan E, Morgen P von, Chu K, Kapoor A, Maciejowski J: **ER-directed TREX1 limits cGAS activation at micronuclei**. *Mol Cell* 2021, doi:10.1016/j.molcel.2020.12.037.

27. Maciejowski J, Chatzipli A, Dananberg A, Chu K, Toufektchan E, Klimczak LJ, Gordenin DA, Campbell PJ, Lange T de: **APOBEC3-dependent kataegis and TREX1-driven chromothripsis during telomere crisis**. *Nat Genet* 2020, **52**:884–890.

28. Lin Y-F, Hu Q, Mazzagatti A, Valle-Inclán JE, Maurais EG, Dahiya R, Guyer A, Sanders JT, Engel JL, Nguyen G, et al.: **Mitotic clustering of pulverized chromosomes from micronuclei**. *Nature* 2023, **618**:1041–1048.

29. Zhang C-Z, Spektor A, Cornils H, Francis JM, Jackson EK, Liu S, Meyerson M, Pellman D: **Chromothripsis from DNA damage in micronuclei**. *Nature* 2015, **522**:179.

30. Mazzagatti A, Engel JL, Ly P: **Boveri and beyond: Chromothripsis and genomic instability from mitotic errors**. *Mol Cell* 2023, doi:10.1016/j.molcel.2023.11.002.

31. Ly P, Cleveland DW: **Rebuilding Chromosomes After Catastrophe: Emerging Mechanisms of Chromothripsis**. *Trends Cell Biol* 2017, **27**:917–930.

32. Mackenzie KJ, Carroll P, Martin C-A, Murina O, Fluteau A, Simpson DJ, Olova N, Sutcliffe H, Rainger JK, Leitch A, et al.: **cGAS surveillance of micronuclei links genome instability to innate immunity**. *Nature* 2017, **548**:461.

33. Harding SM, Benci JL, Irianto J, Discher DE, Minn AJ, Greenberg RA: **Mitotic progression following DNA damage enables pattern recognition within micronuclei**. *Nature* 2017, **548**:466.

34. Flynn PJ, Koch PD, Mitchison TJ: **Chromatin bridges, not micronuclei, activate cGAS after drug-induced mitotic errors in human cells**. *Proc Natl Acad Sci* 2021, **118**:e2103585118.

35. Dou Z, Ghosh K, Vizioli MG, Zhu J, Sen P, Wangensteen KJ, Simithy J, Lan Y, Lin Y, Zhou Z, et al.: **Cytoplasmic chromatin triggers inflammation in senescence and cancer**. *Nature* 2017, **550**:402–406.

36. Guey B, Wischnewski M, Decout A, Makasheva K, Kaynak M, Sakar MS, Fierz B, Ablasser A: **BAF restricts cGAS on nuclear DNA to prevent innate immune activation**. *Science* 2020, **369**:823–828.

37. MacDonald KM, Nicholson-Puthenveedu S, Tageldein MM, Khasnis S, Arrowsmith CH, Harding SM: **Antecedent chromatin organization determines cGAS recruitment to ruptured micronuclei**. *Nat Commun* 2023, **14**:556.

38. Krupina K, Goginashvili A, Cleveland DW: **Causes and consequences of micronuclei**. *Curr Opin Cell Biol* 2021, **70**:91–99.

39. Mammel AE, Hatch EM: **Genome instability from nuclear catastrophe and DNA damage**. *Semin Cell Dev Biol* 2022, **123**:131–139.

40. Papathanasiou S, Mynhier NA, Liu S, Brunette G, Stokasimov E, Jacob E, Li L, Comenho C, Steensel B van, Buenrostro JD, et al.: **Heritable transcriptional defects from aberrations of nuclear architecture**. *Nature* 2023, **619**:184–192.

41. Agustinus AS, Al-Rawi D, Dameracharla B, Raviram R, Jones BSCL, Stransky S, Scipioni L, Luebeck J, Bona MD, Norkunaite D, et al.: **Epigenetic dysregulation from chromosomal transit in micronuclei**. *Nature* 2023, **619**:176–183.

42. Mammel AE, Huang HZ, Gunn AL, Choo E, Hatch EM: **Chromosome length and gene density contribute to micronuclear membrane stability**. *Life Sci Alliance* 2022, **5**:e202101210.

43. Friedrich A, Assmann A-S, Schumacher L, Stuijvenberg J v., Kassack MU, Schulz WA, Roos WP, Hansen FK, Pflieger M, Kurz T, et al.: **In Vitro Assessment of the Genotoxic Hazard of Novel Hydroxamic Acid- and Benzamide-Type Histone Deacetylase Inhibitors (HDACi)**. *Int J Mol Sci* 2020, **21**:4747.

44. Fauth E, Scherthan H: **Frequencies of occurence of all human chromosomes in micronuclei from normal and 5-azacytidine-treated lymphocytes as revealed by chromosome painting**. *Mutagenesis* 1998, **13**:235–241.

45. DiPeso L, Pendyala S, Huang HZ, Fowler DM, Hatch EM: **Machine vision reveals micronucleus rupture as a potential driver of the transcriptomic response to aneuploidy**. *bioRxiv* 2023, doi:10.1101/2023.05.04.539483.

46. Santaguida S, Richardson A, Iyer DR, M’Saad O, Zasadil L, Knouse KA, Wong YL, Rhind N, Desai A, Amon A: **Chromosome Mis-segregation Generates Cell-Cycle-Arrested Cells with Complex Karyotypes that Are Eliminated by the Immune System**. *Dev Cell* 2017, **41**:638-651.e5.

47. He Q, Au B, Kulkarni M, Shen Y, Lim KahJ, Maimaiti J, Wong ChengKit, Luijten MoniqueNH, Chong HC, Lim EH, et al.: **Chromosomal instability-induced senescence potentiates cell non-autonomous tumourigenic effects**. *Oncogenesis* 2018, **7**:62.

48. Hoffelder DR, Luo L, Burke NA, Watkins SC, Gollin SM, Saunders WS: **Resolution of anaphase bridges in cancer cells**. *Chromosoma* 2004, **112**:389–397.

49. Okamoto A, Utani K, Shimizu N: **DNA replication occurs in all lamina positive micronuclei, but never in lamina negative micronuclei**. *Mutagenesis* 2012, **27**:323–327.

50. Crasta K, Ganem NJ, Dagher R, Lantermann AB, Ivanova EV, Pan Y, Nezi L, Protopopov A, Chowdhury D, Pellman D: **DNA breaks and chromosome pulverization from errors in mitosis**. *Nature* 2012, **482**:53.

51. Hatch EM, Fischer AH, Deerinck TJ, Hetzer MW: **Catastrophic Nuclear Envelope Collapse in Cancer Cell Micronuclei**. *Cell* 2013, **154**:47–60.

52. Soto M, García-Santisteban I, Krenning L, Medema RH, Raaijmakers JA: **Chromosomes trapped in micronuclei are liable to segregation errors**. *J Cell Sci* 2018, **131**:jcs.214742.

53. He B, Gnawali N, Hinman AW, Mattingly AJ, Osimani A, Cimini D: **Chromosomes missegregated into micronuclei contribute to chromosomal instability by missegregating at the next division**. *Oncotarget* 2019, **10**:2660–2674.

54. Terradas M, Martín M, Hernández L, Tusell L, Genescà A: **Nuclear envelope defects impede a proper response to micronuclear DNA lesions**. *Mutat Res Fundam Mol Mech Mutagen* 2012, **729**:35–40.

55. Kopito RB, Elbaum M: **Nucleocytoplasmic transport: A thermodynamic mechanism**. *HFSP J* 2009, **3**:130–141.

56. Timney BL, Raveh B, Mironska R, Trivedi JM, Kim SJ, Russel D, Wente SR, Sali A, Rout MP: **Simple rules for passive diffusion through the nuclear pore complex**. *J Cell Biol* 2016, **215**:57–76.

57. Rempel IL, Crane MM, Thaller DJ, Mishra A, Jansen DP, Janssens G, Popken P, Akşit A, Kaeberlein M, Giessen E van der, et al.: **Age-dependent deterioration of nuclear pore assembly in mitotic cells decreases transport dynamics**. *eLife* 2019, **8**:e48186.

58. Snow CJ, Dar A, Dutta A, Kehlenbach RH, Paschal BM: **Defective nuclear import of Tpr in Progeria reflects the Ran sensitivity of large cargo transport**. *J Cell Biol* 2013, **201**:541–557.

59. Timney BL, Tetenbaum-Novatt J, Agate DS, Williams R, Zhang W, Chait BT, Rout MP: **Simple kinetic relationships and nonspecific competition govern nuclear import rates in vivo**. *J Cell Biol* 2006, **175**:579–593.

60. Yang W, Musser SM: **Nuclear import time and transport efficiency depend on importin β concentration**. *J Cell Biol* 2006, **174**:951–961.

61. Windner SE, Manhart A, Brown A, Mogilner A, Baylies MK: **Nuclear Scaling Is Coordinated among Individual Nuclei in Multinucleated Muscle Fibers**. *Dev Cell* 2019, **49**:48-62.e3.

62. Sepaniac LA, Martin W, Dionne LA, Stearns TM, Reinholdt LG, Stumpff J: **Micronuclei in Kif18a mutant mice form stable micronuclear envelopes and do not promote tumorigenesis**. *J Cell Biol* 2021, **220**:e202101165.

63. Pfeifer CR, Tobin MP, Cho S, Vashisth M, Dooling LJ, Vazquez LL, Lucca EGR-D, Simon KT, Discher DE: **Gaussian curvature dilutes the nuclear lamina, favoring nuclear rupture, especially at high strain rate**. *Nucleus* 2022, **13**:129–143.

64. Almeida M de, Hinterndorfer M, Brunner H, Grishkovskaya I, Singh K, Schleiffer A, Jude J, Deswal S, Kalis R, Vunjak M, et al.: **AKIRIN2 controls the nuclear import of proteasomes in vertebrates**. *Nature* 2021, **599**:491–496.

65. Dopie J, Skarp K-P, Rajakylä EK, Tanhuanpää K, Vartiainen MK: **Active maintenance of nuclear actin by importin 9 supports transcription**. *Proc Natl Acad Sci* 2012, **109**:E544–E552.

66. Worrall JT, Tamura N, Mazzagatti A, Shaikh N, Lingen T van, Bakker B, Spierings DCJ, Vladimirou E, Foijer F, McClelland SE: **Non-random Mis-segregation of Human Chromosomes**. *Cell Reports* 2018, **23**:3366–3380.

67. Drpic D, Almeida AC, Aguiar P, Renda F, Damas J, Lewin HA, Larkin DM, Khodjakov A, Maiato H: **Chromosome Segregation Is Biased by Kinetochore Size**. *Curr Biol* 2018, **28**:1344-1356.e5.

68. Klaasen SJ, Truong MA, Jaarsveld RH van, Koprivec I, Štimac V, Vries SG de, Risteski P, Kodba S, Vukušić K, Luca KL de, et al.: **Nuclear chromosome locations dictate segregation error frequencies**. *Nature* 2022, doi:10.1038/s41586-022-04938-0.

69. Dumont M, Gamba R, Gestraud P, Klaasen S, Worrall JT, Vries SGD, Boudreau V, Salinas-Luypaert C, Maddox PS, Lens SM, et al.: **Human chromosome-specific aneuploidy is influenced by DNA-dependent centromeric features**. *Embo J* 2020, **39**:e102924.

70. Orr B, Sousa FD, Gomes AM, Afonso O, Ferreira LT, Figueiredo AC, Maiato H: **An anaphase surveillance mechanism prevents micronuclei formation from frequent chromosome segregation errors**. *Cell Reports* 2021, **37**:109783.

71. MacDonald KM, Khan S, Kislinger T, Harding SM: **The proteomic landscape of genotoxic stress-induced micronuclei**. *bioRxiv* 2023, doi:10.1101/2023.08.27.555027.

72. Chen J, Harding SM, Natesan R, Tian L, Benci JL, Li W, Minn AJ, Asangani IA, Greenberg RA: **Cell Cycle Checkpoints Cooperate to Suppress DNA- and RNA-Associated Molecular Pattern Recognition and Anti-Tumor Immune Responses**. *Cell Rep* 2020, **32**:108080.

73. Stephens AD, Liu PZ, Banigan EJ, Almassalha LM, Backman V, Adam SA, Goldman RD, Marko JF: **Chromatin histone modifications and rigidity affect nuclear morphology independent of lamins**. *Mol Biol Cell* 2018, **29**:220–233.

74. Parker M, Mohankumar KM, Punchihewa C, Weinlich R, Dalton JD, Li Y, Lee R, Tatevossian RG, Phoenix TN, Thiruvenkatam R, et al.: **C11orf95–RELA fusions drive oncogenic NF-κB signalling in ependymoma**. *Nature* 2014, **506**:451–455.

75. Zych MG, Hatch EM: **Small spaces, big problems: The abnormal nucleoplasm of micronuclei and its consequences**. *Curr Opin Struct Biol* 2024, **87**:102839.

76. Ly P, Teitz LS, Kim DH, Shoshani O, Skaletsky H, Fachinetti D, Page DC, Cleveland DW: **Selective Y centromere inactivation triggers chromosome shattering in micronuclei and repair by non-homologous end joining**. *Nat Cell Biol* 2016, **19**:68–75.

77. Nader GP de F, Agüera-Gonzalez S, Routet F, Gratia M, Maurin M, Cancila V, Cadart C, Palamidessi A, Ramos RN, Roman MS, et al.: **Compromised nuclear envelope integrity drives TREX1-dependent DNA damage and tumor cell invasion**. *Cell* 2021, doi:10.1016/j.cell.2021.08.035.

78. Afonso O, Figueiredo AC, Maiato H: **Late mitotic functions of Aurora kinases**. *Chromosoma* 2017, **126**:93–103.

79. Ivanovska IL, Tobin MP, Bai T, Dooling LJ, Discher DE: **Small lipid droplets are rigid enough to indent a nucleus, dilute the lamina, and cause rupture**. *J Cell Biology* 2023, **222**:e202208123.

80. Berg IK, Currey ML, Gupta S, Berrada Y, Nguyen BV, Pho M, Patteson AE, Schwarz JM, Banigan EJ, Stephens AD: **Transcription inhibition suppresses nuclear blebbing and rupture independent of nuclear rigidity**. *J Cell Sci* 2023, **136**.

81. Krause M, Riet J te, Wolf K: **Probing the compressibility of tumor cell nuclei by combined atomic force–confocal microscopy**. *Phys Biol* 2013, **10**:065002.

82. Cavazza T, Vernos I: **The RanGTP Pathway: From Nucleo-Cytoplasmic Transport to Spindle Assembly and Beyond**. *Front Cell Dev Biol* 2016, **3**:82.

83. Schaik T van, Vos M, Peric-Hupkes D, Celie PH, Steensel B van: **Cell cycle dynamics of lamina-associated DNA**. *Embo Rep* 2020, **21**:e50636.

84. Kiyomitsu T, Cheeseman IM: **Chromosome- and spindle-pole-derived signals generate an intrinsic code for spindle position and orientation**. *Nat Cell Biol* 2012, **14**:311–317.

85. Jevtić P, Schibler AC, Wesley CC, Pegoraro G, Misteli T, Levy DL: **The nucleoporin ELYS regulates nuclear size by controlling NPC number and nuclear import capacity**. *Embo Rep* 2019, **20**.

86. Jevtić P, Edens LJ, Li X, Nguyen T, Chen P, Levy DL: **Concentration-dependent Effects of Nuclear Lamins on Nuclear Size in Xenopus and Mammalian Cells***. *J Biol Chem* 2015, **290**:27557–27571.

87. Levy DL, Heald R: **Nuclear Size Is Regulated by Importin α and Ntf2 in Xenopus**. *Cell* 2010, **143**:288–298.

88. Niopek D, Wehler P, Roensch J, Eils R, Ventura BD: **Optogenetic control of nuclear protein export**. *Nat Commun* 2016, **7**:10624.

89. Tachibana *Taro, Hieda M, Miyamoto Y, Kose S, Imamoto N, Yoneda Y: **Recycling of Importin α from the Nucleus Is Suppressed by Loss of RCC1 Function in Living Mammalian Cells**. *Cell Struct Funct* 2000, **25**:115–123.

90. Dworak N, Makosa D, Chatterjee M, Jividen K, Yang C, Snow C, Simke WC, Johnson IG, Kelley JB, Paschal BM: **A nuclear lamina-chromatin-Ran GTPase axis modulates nuclear import and DNA damage signaling**. *Aging Cell* 2019, **18**:e12851.

91. Cortés-Ciriano I, Lee JJ-K, Xi R, Jain D, Jung YL, Yang L, Gordenin D, Klimczak LJ, Zhang C-Z, Pellman DS, et al.: **Comprehensive analysis of chromothripsis in 2,658 human cancers using whole-genome sequencing**. *Nat Genet* 2020, **52**:331–341.

92. Maciejowski J, Li Y, Bosco N, Campbell PJ, de Lange T: **Chromothripsis and Kataegis Induced by Telomere Crisis**. *Cell* 2015, **163**:1641–1654.

93. Hatch EM, Hetzer MW: **Nuclear envelope rupture is induced by actin-based nucleus confinement**. *J Cell Biol* 2016, **215**:27–36.

94. Hoff DDV, McGill JR, Forseth BJ, Davidson KK, Bradley TP, Devanter DRV, Wahl GM: **Elimination of extrachromosomally amplified MYC genes from human tumor cells reduces their tumorigenicity.** *Proc Natl Acad Sci* 1992, **89**:8165–8169.

95. Shimizu N: **Molecular mechanisms of the origin of micronuclei from extrachromosomal elements**. *Mutagenesis* 2011, **26**:119–123.

96. Young AM, Gunn AL, Hatch EM: **BAF facilitates interphase nuclear membrane repair through recruitment of nuclear transmembrane proteins**. *Mol Biol Cell* 2020, **31**:1551–1560.

97. Schindelin J, Arganda-Carreras I, Frise E, Kaynig V, Longair M, Pietzsch T, Preibisch S, Rueden C, Saalfeld S, Schmid B, et al.: **Fiji: an open-source platform for biological-image analysis**. *Nat Methods* 2012, **9**:676–682.

98. Gunn AL, Yashchenko AI, Dubrulle J, Johnson J, Hatch EM: **A high-content screen reveals new regulators of nuclear membrane stability**. *Sci Rep* 2024, **14**:6013.

99. Consortium TIP-CA of WG, Aaltonen LA, Abascal F, Abeshouse A, Aburatani H, Adams DJ, Agrawal N, Ahn KS, Ahn S-M, Aikata H, et al.: **Pan-cancer analysis of whole genomes.** *Nature* 2018, **578**:82–93.

100. Islam SMA, Díaz-Gay M, Wu Y, Barnes M, Vangara R, Bergstrom EN, He Y, Vella M, Wang J, Teague JW, et al.: **Uncovering novel mutational signatures by de novo extraction with SigProfilerExtractor**. *Cell Genom* 2022, **2**:100179.

101. Bakhoum SF, Ngo B, Laughney AM, Cavallo J-A, Murphy CJ, Ly P, Shah P, Sriram RK, Watkins TBK, Taunk NK, et al.: **Chromosomal instability drives metastasis through a cytosolic DNA response**. *Nature* 2018, **553**:467.

102. Malhotra A, Lindberg M, Faust GG, Leibowitz ML, Clark RA, Layer RM, Quinlan AR, Hall IM: **Breakpoint profiling of 64 cancer genomes reveals numerous complex rearrangements spawned by homology-independent mechanisms**. *Genome Res* 2013, **23**:762–776.

103. Rausch T, Jones DTW, Zapatka M, Stütz AM, Zichner T, Weischenfeldt J, Jäger N, Remke M, Shih D, Northcott PA, et al.: **Genome Sequencing of Pediatric Medulloblastoma Links Catastrophic DNA Rearrangements with TP53 Mutations**. *Cell* 2012, **148**:59–71.

104. Molenaar JJ, Koster J, Zwijnenburg DA, Sluis P van, Valentijn LJ, Ploeg I van der, Hamdi M, Nes J van, Westerman BA, Arkel J van, et al.: **Sequencing of neuroblastoma identifies chromothripsis and defects in neuritogenesis genes**. *Nature* 2012, **483**:589–593.

105. Stephens PJ, Greenman CD, Fu B, Yang F, Bignell GR, Mudie LJ, Pleasance ED, Lau KW, Beare D, Stebbings LA, et al.: **Massive Genomic Rearrangement Acquired in a Single Catastrophic Event during Cancer Development**. *Cell* 2011, **144**:27–40.

106. Norppa H, Falck GC-M: **What do human micronuclei contain?** *Mutagenesis* 2003, **18**:221–233.

107. Catalán J, Falck GC-M, Norppa H: **The X Chromosome Frequently Lags Behind in Female Lymphocyte Anaphase**. *Am J Hum Genetics* 2000, **66**:687–691.

108. Tucker JD, Nath J, Hando JC: **Activation status of the X chromosome in human micronucleated lymphocytes**. *Hum Genet* 1996, **97**:471–475.

109. Thompson SL, Bakhoum SF, Compton DA: **Mechanisms of Chromosomal Instability**. *Curr Biol* 2010, **20**:R285–R295.

110. Gregan J, Polakova S, Zhang L, Tolić-Nørrelykke IM, Cimini D: **Merotelic kinetochore attachment: causes and effects**. *Trends Cell Biol* 2011, **21**:374–381.

111. Lara-Gonzalez P, Westhorpe FG, Taylor SS: **The Spindle Assembly Checkpoint**. *Curr Biol* 2012, **22**:R966–R980.

112. Iwanaga Y, Chi Y-H, Miyazato A, Sheleg S, Haller K, Peloponese J-M, Li Y, Ward JM, Benezra R, Jeang K-T: **Heterozygous Deletion of Mitotic Arrest–Deficient Protein 1 (MAD1) Increases the Incidence of Tumors in Mice**. *Cancer Res* 2007, **67**:160–166.

113. Michel LS, Liberal V, Chatterjee A, Kirchwegger R, Pasche B, Gerald W, Dobles M, Sorger PK, Murty VVVS, Benezra R: **MAD2 haplo-insufficiency causes premature anaphase and chromosome instability in mammalian cells**. *Nature* 2001, **409**:355–359.

114. Baker DJ, Dawlaty MM, Wijshake T, Jeganathan KB, Malureanu L, Ree JH van, Crespo-Diaz R, Reyes S, Seaburg L, Shapiro V, et al.: **Increased expression of BubR1 protects against aneuploidy and cancer and extends healthy lifespan**. *Nat Cell Biol* 2013, **15**:96–102.

115. Aguilar R, Camplisson CK, Lin Q, Miga KH, Noble WS, Beliveau BJ: **Tigerfish designs oligonucleotide-based in situ hybridization probes targeting intervals of highly repetitive DNA at the scale of genomes**. *Nat Commun* 2024, **15**:1027.

116. Kishi JY, Lapan SW, Beliveau BJ, West ER, Zhu A, Sasaki HM, Saka SK, Wang Y, Cepko CL, Yin P: **SABER amplifies FISH: enhanced multiplexed imaging of RNA and DNA in cells and tissues**. *Nat Methods* 2019, **16**:533–544.

117. Cremer T, Cremer M: **Chromosome Territories**. *Csh Perspect Biol* 2010, **2**:a003889.

118. Adam SA, Sterne-Marr R, Gerace L: **[11] Nuclear protein import using digitonin-permeabilized cells**. *Methods Enzym* 1992, **219**:97–110.

119. Hayes LR, Duan L, Bowen K, Kalab P, Rothstein JD: **C9orf72 arginine-rich dipeptide repeat proteins disrupt karyopherin-mediated nuclear import**. *eLife* 2020, **9**:e51685.

120. Moore WJ, Zhang C, Clarke PR: **Targeting of RCC1 to Chromosomes Is Required for Proper Mitotic Spindle Assembly in Human Cells**. *Curr Biol* 2002, **12**:1442–1447.

121. Clarke PR, Zhang C: **Spatial and temporal coordination of mitosis by Ran GTPase**. *Nat Rev Mol Cell Bio* 2008, **9**:464–477.

122. Nemergut ME, Macara IG: **Nuclear Import of the Ran Exchange Factor, Rcc1, Is Mediated by at Least Two Distinct Mechanisms**. *J Cell Biology* 2000, **149**:835–850.

Appendix A: Supplementary material for Chapter 2

Supplementary Figures

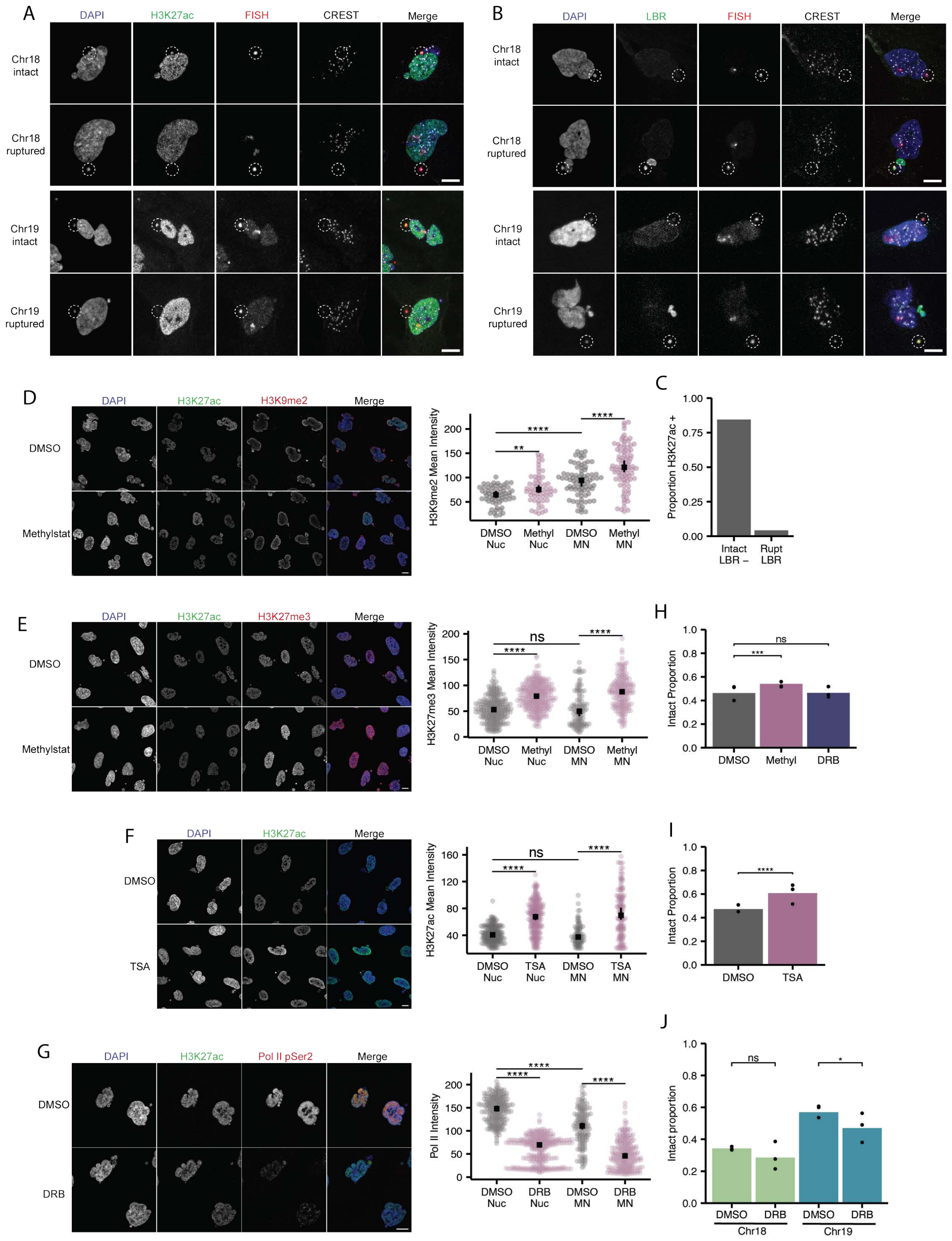

Supplementary Figure 2.1: Manipulation of histone modifications and transcription in nuclei and MN

A. Maximum intensity projection images of intact (H3K27ac+) and ruptured (H3K27ac-) MN in RPE-1 cells containing a single copy (1 CREST focus) of chr18 or 19. **B.** Maximum intensity projection images of intact (LBR-) and ruptured (LBR+) MN in RPE-1 cells containing a single copy (1 CREST focus) of chr18 or 19. Scale bar for A and B = 10um. **C.** Quantification of H3K27ac and LBR colocalization in RPE-1 cells 84.5% LBR- MN were of H3K27ac+ and 4.3% of LBR+ MN were of H3K27ac+. N=3, n=620. **D,E**. Example images of H3K9me2 and H3K27me3 staining in nuclei and MN from RPE-1 cells with single sections shown. Quantification of H3K9me2 and H3K27me3 intensity in nuclei and intact (H3K27ac+) MN in cell treatment with DMSO and 5um methylstat. Scale bar = 10um. C. H3K9me2 Wilcoxon ran sum test, N=3, n=(62,58,82,86) D. H3K27me3 Wilcoxon ran sum test, N=3, n=(231, 269, 109, 177). **F.** Example images of H3K27ac staining nuclei and MN from RPE-1 cells with single sections shown. Quantification of H3K27ac in nuclei and micronuclei in cells treated with DMSO and 100nm TSA. Scale bar = 10um. Wilcoxon ran sum test. N=3, n=(224, 252, 93, 149). **G**. Example images of Pol II pSer2 staining in nuclei and MN from RPE-1 cells with single sections shown. Quantification of Pol II pSer2 intensity in nuclei and intact (H3K27ac+) MN in cells treated with DMSO and 100ug/ml DRB. Wilcoxon ran sum test. N=3, n=(210,267,136,220). **H.** Intact proportion of bulk MN 24hr post BAY determined by H3K27ac classification in cells treated with DMSO, 5uM methylstat, and 100ug/ml DRB. Barnards test, N=3, n=(477,432, 386). **I.** intact proportion of bulk MN 24hr post BAY determined by LBR classification in cells treated with DMSO and 100nm TSA. Barnards test, N=3, n=(462, 560). **J.** Intact proportion of 24hr post BAY release single chromosomes chr18 and 19 MN after DMSO and 100ug/ml DRB treatment. Barnards test, N=3, n=(216,147,165, 304). For all graphs, ns p>0.05, * p<0.05, ** p<0.01, *** p<0.001, **** p<0.0001.

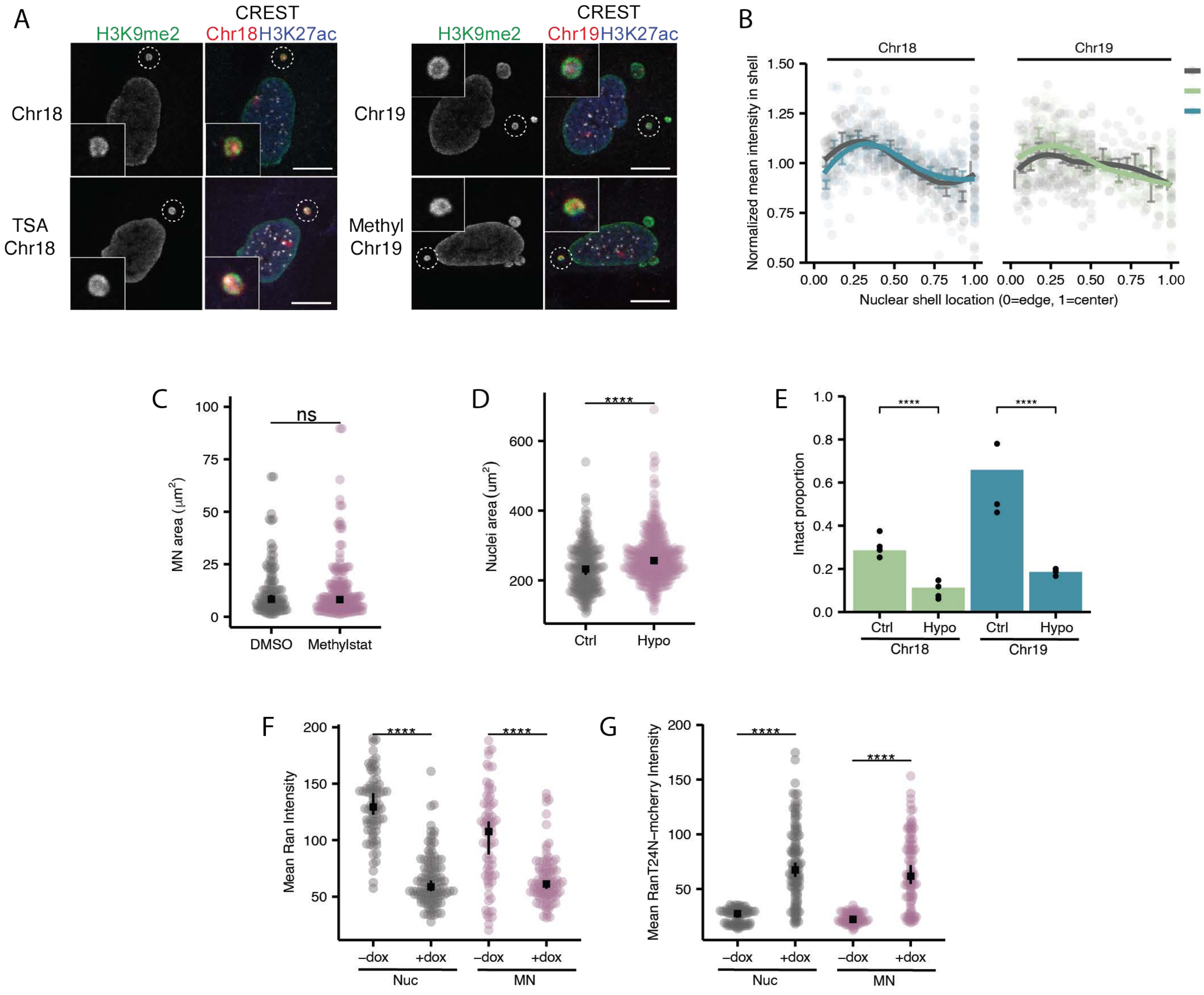

Supplementary Figure 2.2: Lamina gaps and instability in MN correlate with growth not LADs

A. Example images of H3K9me2 staining in single chromomsome 18 and 19 RPE-1 cell MN treated with DMSO , 5uM methylstat, or 100nm TSA with single sections shown. Scale bar = 10um. **B.** Chr18 and 19 MN from A were segmented into 1um thick concentric shells and the mean H3K9me2 intensity was quantified in each shell N=3, chr 18 n=(30, 34), chr19 n=(29, 30). **C.** Max projected area for bulk intact MN in RPE-1 cells treated with DMSO and 5uM methystat for 4 hours. N=3, n=(268, 276). **D.** Maximum projected area of nuclei in RPE-1 control cells and after hypotonic swelling in media diluted 1:2 in sterile H2O for 1 hour. Wilcoxon rank sum test, N= 3, n=(233, 377). **E.** MN stability for single chromosome 18 or 19 MN in RPE-1 cells 24hrs after BAY for control and hypotonic treated cells. Barnards test, N=3, n=(224, 169, 85, 70). **F.** Quantification of Ran staining in nuclei and intact MN in RPE-1 TetOn Tre-RanT24N-mcherry cells treated with 0ng/ul and 100ng/ul dox. Wilcoxon rank sum, N=3, n=(79,113,72,97). **G.** Quantification of RanT24N-mcherry staining in nuclei and intact MN in RPE-1 TetOn Tre-RanT24N-mcherry cells treated with 0ng/ul and 100ng/ul dox. Wilcoxon rank sum, N=3, n=(79,113,72,97). For all graphs, ns p>0.05, * p<0.05, ** p<0.01, *** p<0.001, **** p<0.0001.

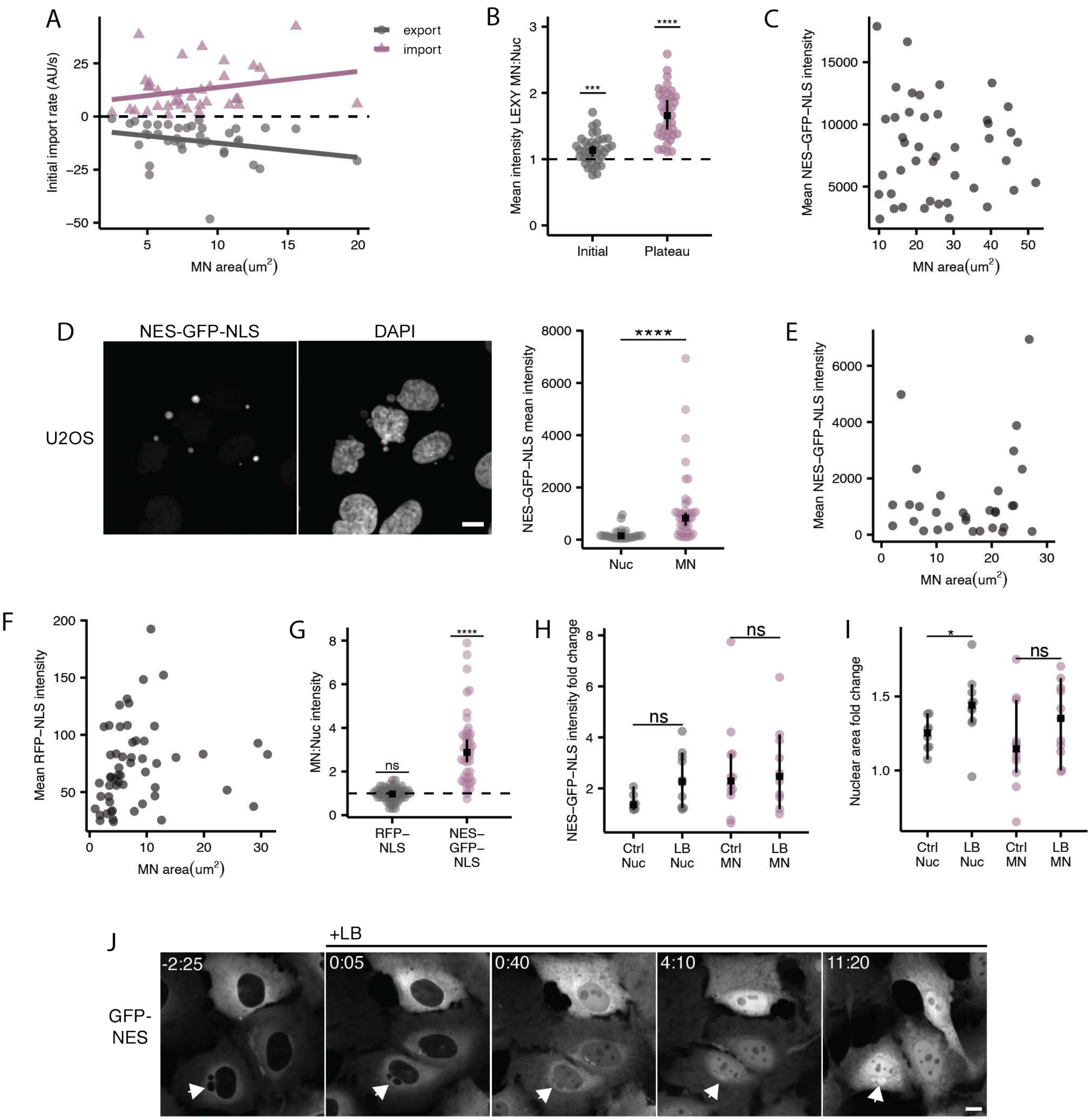

Supplementary Figure 2.3: MN transport rates are conserved and not correlated with MN area

A. Nuclear import and export rates quantified form LEXY intensity changes are not correlated with MN area. **B.** LEXY-mcherry intensity quantified in MN and nuclei at the start of imagine in the absence of UV (initial) and after 45 min of UV exposure to induce export (plateau). MN were compared to their corresponding nuclei. One-sample Wilcoxon rank sum test, N=3, n=(34). **C.** NES-GFP-NLS intensity levels quantified in RPE-1 cell MN are not correlated with MN area. Spearman correlation R= 0.014, p=0.93. **D.** Maximum projection images of U2OS cells expressing NES-GFP-NLS. Scale bar = 10um. NES-GFP-NLS intensity was quantified for nuclei and intact MN in U2OS cells. Wilcoxon rank sum, N=1 n=(25, 41) **E.** NES-GFP-NLS intensity levels quantified in U2OS cell MN are not correlated with MN area. Spearman correlation R=-0.25, p=0.55. **F.** RFP-NLS intensity levels quantified in RPE-1 cell MN are not correlated with MN area. Spearman correlation R= 0.35, p=0.0081**. G.** MN:Nuc ratios for RFP-NLS and NES-GFP-NLS intensity quantified in RPE-1 cells. One-sample Wilcoxon rank sum test, N=3,1, n=(55,43). **H,I.** The intensity of NES-GFP-NLS and area for nuclei and intact MN measured from live imaging of RPE-1 cells expressing NES-GFP-NLS at the start of imaging and 5hrs after 20ng/ul leptB LB addition. The fold change of area and intensity over 5hrs was calculated. Wilcoxon rank sum test, N=1, Nuc n=36, MN n=46. **J.** Live imaging of U2OS cells expressing GFP-NES with single sections shown. Cells imaged every 5 minutes. Arrowheads show MN that exclude GFP-NES before leptB addition and accumulate GFP-NES after leptB addition. Intensity min and max were reset to better visualize localization at each timepoint. Scale bar= 10 um. Time shown as hr:min.For all graphs, ns $p>0.05$, * $p<0.05$, ** $p<0.01$, *** $p<0.001$, **** $p<0.0001$.

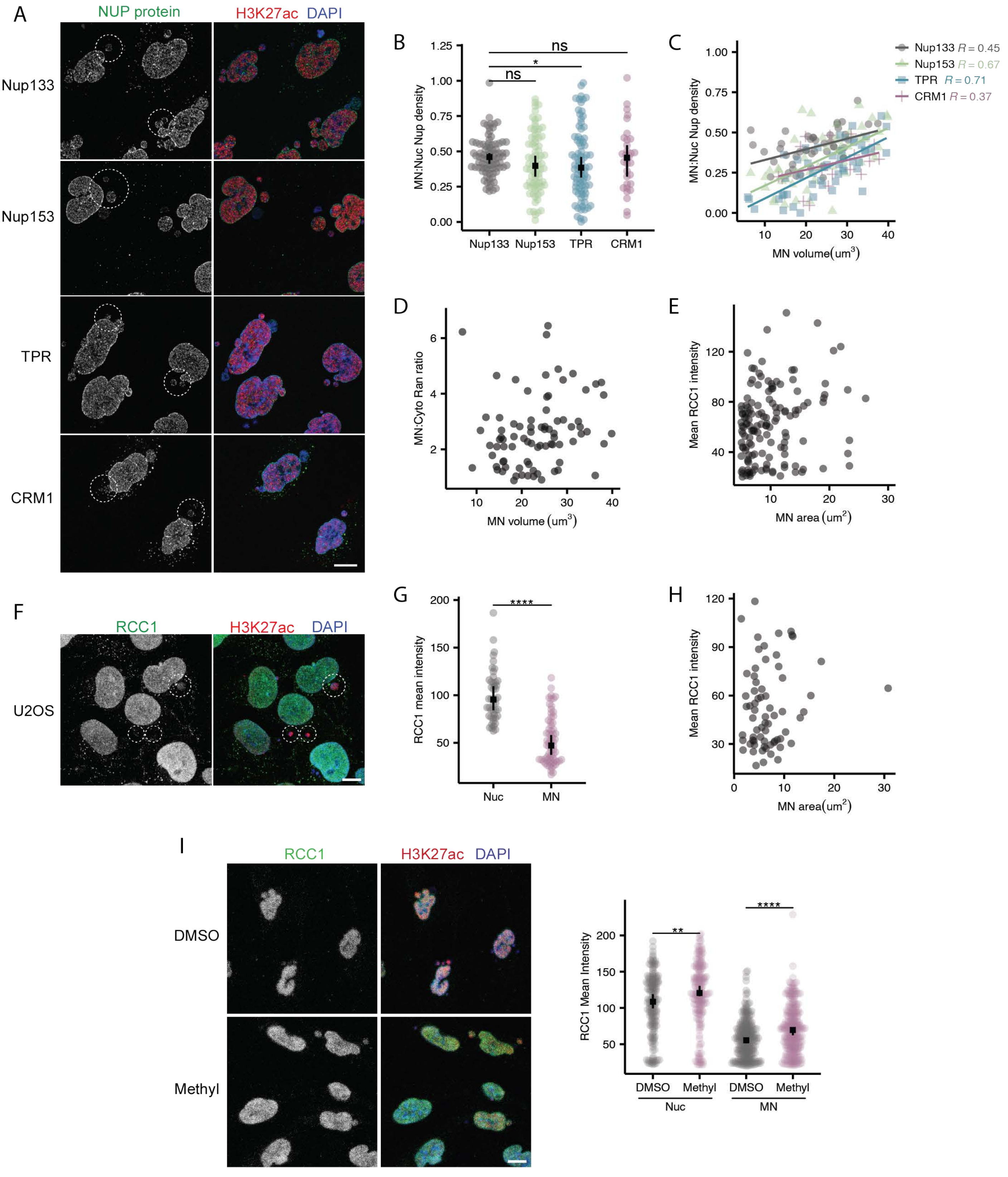
A
NUP protein
H3K27ac DAPI
Nup133
Nup153
TPR
CRM1
B
MN:Nuc Nup density
1.25
1.00
0.75
0.50
0.25
0.00
ns
*
ns
Nup133
Nup153
TPR
CRM1
C
MN:Nuc Nup density
1.00
0.75
0.50
0.25
0.00
10
20
30
40
MN volume(um^3)
Nup133 $R = 0.45$
Nup153 $R = 0.67$
TPR $R = 0.71$
CRM1 $R = 0.37$
D
MN:Cyto Ran ratio
6
4
2
10
20
30
40
MN volume (um^3)
E
Mean RCC1 intensity
120
80
40
10
20
30
MN area (um^2)
F
RCC1
H3K27ac DAPI
U2OS
G
RCC1 mean intensity
200
150
100
50
****
Nuc
MN
H
Mean RCC1 intensity
120
90
60
30
0
10
20
30
MN area(um^2)
I
RCC1
H3K27ac DAPI
DMSO
Methyl
RCC1 Mean Intensity
200
150
100
50
**
****
DMSO
Methyl
DMSO
Methyl
Nuc
MN

Supplementary Figure 2.4: RCC1 levels more than NUP density correlate with export defects in MN

A. Maximum projections of the top surface of nuclei and MN in RPE-1 cells stained for Nup133, Nup153, TPR, and CRM1. Intact MN indicated by white circles. Scale bar =10um. **B.** Quantification of NUP density for images in A. Wilcoxon rank sum test, N=(3,3,3,1), n=(84,76,84,32). One sample Wilcoxon rank sum comparing MN:Nuc to 1, Nup133 $p<0.0001$, Nup153 $p<0.0001$, TPR $p<0.0001$, CRM1 $p<0.0001$. **C.** Correlation between NUP density and MN volume for quantification in B. R= Spearman correlation coefficient. Nup133 $p<0.01$, Nup153 $p<0.0001$, TPR $p<0.0001$, CRM1 $p>0.05$. **D.** Ran intensity levels quantified in RPE-1 cell MN are not correlated with MN area. Spearman coefficient R= 0.26, p=0.0017. **E.** RCC1 intensity levels quantified in RPE-1 cell MN are not correlated with MN area. Spearman coefficient R= 0.24, p=0.0033. **F.** Maximum projected images of RCC1 staining in U2OS cells. Intact MN indicated by white circles. Scale bar= 10um. **G.** Quantification of RCC1 intensity in F for nuclei and intact MN. Wilcoxon ran sum test, N=1, n=(46, 68). **H.** RCC1 intensity in U2OS cell MN is not correlate with MN area. Spearman coefficient R= 0.1, p=0.41. **I.** Images of RCC1 in RPE-1 cells treated with DMSO and 5um methylstat. Single sections shown. Quantification of RCC1 intensity in nuclei and intact MN. Wilcoxon ran sum test, N=3, n=(168, 177, 268, 276). For all graphs, ns $p>0.05$, * $p<0.05$, ** $p<0.01$, *** $p<0.001$, **** $p<0.0001$.

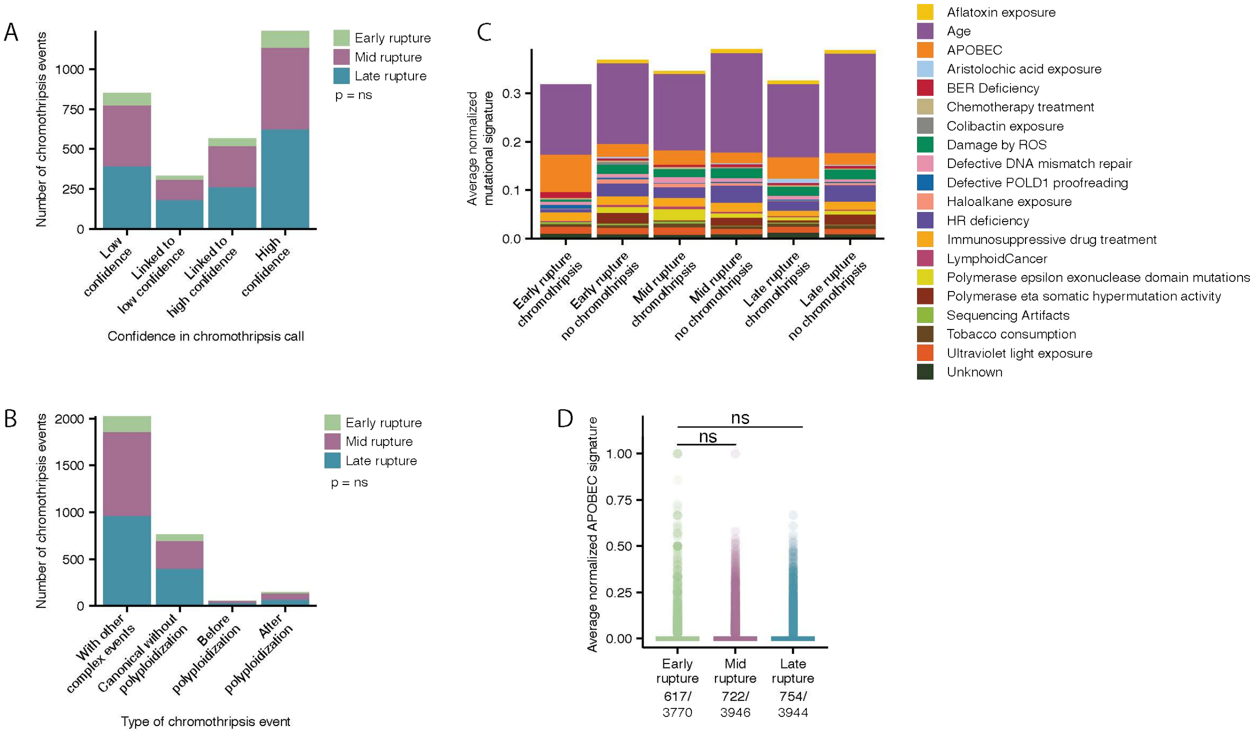

Supplementary Figure 2.5: Controls for chromothripsis analysis

A,B. Chromothripsis calls are not biased by chromosome class. **C.** Mutational signatures are broadly present and identifiable in all chromosome classes, with and without chromothripsis events (labeled as ‘chromothripsis’ or ‘no’). Chi-square test **D.** APOBEC mutational signature is not increased in early rupture chromosomes not involved in chromothripsis events. Anova p= ns. Number of non-zero datapoints out of the total are indicated under each group. n=(3770, 3946, 3944). For all graphs, ns $p>0.05$, * $p<0.05$, ** $p<0.01$, *** $p<0.001$, **** $p<0.0001$.